RMetS
Royal Meteorological Society

The evolution of an MCS over southern England. Part 1: Observations

P. A. Clark,[a]* K. A. Browning,[b] C. J. Morcrette,[c]† A. M. Blyth,[d]
R. M. Forbes,[e] B. Brooks[d] and F. Perry[d]

[a]*Department of Meteorology, University of Reading, UK*
[b]*Independent researcher*
[c]*Met Office, Exeter, UK*
[d]*School of Earth and Environment, University of Leeds, UK*
[e]*ECMWF, Reading, UK*

*Correspondence to: P. A. Clark, Department of Meteorology, University of Reading, PO Box 243, Earley Gate, Reading RG6 6BB, Berkshire, UK. E-mail: p.clark@reading.ac.uk
†The contribution of C. J. Morcrette was written in the course of his employment at the Met Office, UK and is published with the permission of the Controller of HMSO and the Queen's Printer for Scotland.

Observations are described of a Mesoscale Convective System (MCS) with a cold pool which propagated across southern England on 25 August 2005. The observations were made as part of the Convective Storm Initiation Project (CSIP).

The observed MCS structure broadly followed well-established theories, including the presence of a weak rear-inflow jet. In detail, however, unsteady transitions occurred involving the formation of two distinct lines of showers ahead of the initial linear system. In each case the cold pool merged with cold downdraughts from the new showers leading to a discontinuous propagation of the system. One of these lines formed independently of the MCS, very probably on a sea-breeze convergence line. The mechanism for formation of the other is unknown, but it is possible that it was triggered by ascent associated with gravity waves generated by the MCS. The merged cold pool was deeper and colder and propagated faster than the original system, eventually forming a bow echo and arc cloud as it propagated across the English Channel. Until completion of the merger, the propagation velocity of the overall system had been controlled by a combination of the above mechanisms rather than simply by cold pool dynamics.

Key Words: convection; precipitation; cold pool; rear-inflow jet; cloud microphysics

Received 13 September 2012; Revised 25 January 2013; Accepted 13 February 2013; Published online in Wiley Online Library 13 May 2013

Citation: Clark PA, Browning KA, Morcrette CJ, Blyth AM, Forbes RM, Brooks B, Perry F. 2014. The evolution of an MCS over southern England. Part 1: Observations. *Q. J. R. Meteorol. Soc.* **140**: 439–457. DOI:10.1002/qj.2138

1. Introduction

Severe convective storms are amongst the weather phenomena with greatest impact on society. They may be associated with damage from lightning and strong winds (due to a variety of phenomena including convectively driven gusts and tornadoes) and they generally produce the highest rainfall rates observed. They can lead to rapid ('flash') flooding of small areas. The localised nature and inherent difficulties predicting the precise location of storms often means that flooding occurs with very little warning, leading to severe risk to life and property.

There is thus a considerable need for improved tools to enable the forecasting of convective storms. Nowcasting

systems (e.g. Wilson and Mueller, 1993; Henry and Wilson, 1995; Golding, 1998) make use of rapidly updating observations (primarily radar and geostationary satellites) together with understanding, knowledge of typical precursor signals and extrapolation to make very short-range forecasts. With the advent of non-hydrostatic numerical weather prediction (NWP) models and the affordability of the computer power required to run them at high enough resolution, dynamically based forecasts are becoming increasingly feasible (e.g. Lean *et al.*, 2008), but these will depend on fast and efficient data assimilation systems making use of similar data to nowcasting systems.

The greatest challenge to forecasting convective storms is the prediction of the formation of new storm cells. Understanding is needed of the mechanisms leading both to the formation of initial cells where none existed before (primary initiation) and new cells associated with the flows caused by existing cells (secondary initiation).

This problem has been studied extensively in the past, but mainly over largely flat, continental, terrain (most recently in the IHOP field campaign, Weckwerth *et al.*, 2004) or mountainous, continental, terrain (e.g. during the Mesoscale Alpine Programme (Bougeault *et al.*, 2001, 2002) and the Convective and Orographically-induced Precipitation Study (Wulfmeyer *et al.*, 2008)). The Convective Storm Initiation Project (CSIP) was designed to study convective initiation in a moderately hilly, extratropical maritime environment, representative of much of Northwest Europe and parts of the west coast of North America, as well as the United Kingdom. CSIP was organised to obtain detailed observations of the state of the atmosphere prior to, and during, the early stages of the development of precipitating convection (Browning *et al.*, 2007). The field campaign associated with CSIP was carried out in June, July and August 2005, following a pilot campaign in July 2004 and comprised 18 intensive observation periods (IOPs).

This article describes a synthesis of observations made during CSIP IOP 18, on 25 August 2005. These observations focus on the initiation of secondary cells and inevitably, due to the focus of CSIP, concentrate more on near-surface processes. Part 2 presents further insight gained from model hindcasts of the IOP. The event of greatest interest in IOP 18 is a mesoscale convective system (MCS) with a cold pool.

The mechanisms responsible for convective organisation have been studied for several decades. The structure and dynamics of MCSs was recently comprehensively reviewed by Houze (2004). Convection itself is dominated by fast-manifold dynamics driving updraughts and associated downdraughts. These may produce surface cold pools, and cold-pool dynamics have been identified as contributing to organisation and propagation of MCSs. Rotunno *et al.* (1988) introduced a theory (often referred to as RKW theory) for long-lived squall lines involving the interaction of the surface cold pool with low-level shear; they suggest an optimal condition being that the cold pool propagates as a density current at a speed matching the system velocity. More recently, Tompkins (2001) has suggested a more thermodynamic role of cold pools in organising tropical deep convection.

The convective updraughts and further condensation in the anvil deliver positively buoyant air to the upper troposphere which can modify the mesoscale flow in a number of ways. Weisman (1992) identified the horizontal buoyancy gradient at the rear of a system as being responsible for generating a rear-inflow jet and modified RKW theory to take account its role in the horizontal vorticity budget and thence the propagation of the system, though, like its predecessor, the modified theory could not be described as complete as it does not describe the coupling between dynamics and the thermodynamics of condensation and evaporation (or other microphysical processes). Fujita (1978) introduced the concept of bow echoes which involve similar processes but with additional 3D features (Weisman, 2001).

Any convective disturbance can act as a source of gravity waves due to the bulk upward and downward transport of mass and diabatic heating. The excited waves may cover a variety of wavelengths. Indeed, the large-scale subsidence response can be thought of as a long gravity-wave response. Gravity waves may propagate ahead of a system and thereby modify the inflow conditions (Fovell, 2002), and short gravity waves close to the system may contribute to triggering of new cells ahead (Fovell *et al.*, 2006), especially where small but significant convective inhibition (CIN) may be modified by the waves (Morcrette *et al.*, 2006; Marsham and Parker, 2006). Furthermore, a great deal of work has focussed on propagation mechanisms involving coupling between gravity waves and convection, as summarised by Cram *et al.* (1992), including wave-CISK (convective initiation of the second kind) theories (Raymond, 1984) and the role of upper tropospheric gravity waves in exciting the rear inflow jet (Schmidt and Cotton, 1990). Pandya and Durran (1996) show that key features of two-dimensional squall lines can be accounted for directly from the gravity-wave response to the mean heating profile, largely that arising from the leading edge convection. This includes aspects of the rear-inflow jet, though they also show that this requires the gravity-wave response to be modified by the stability profile of the cold pool. Furthermore, it has been shown that the dominant propagation mechanism may change from low-level cold pool dynamics to upper-level gravity wave dynamics (Bernardet and Cotton, 1998), especially as the boundary layer stabilises at night.

The lifetime of MCSs is often long enough that the Coriolis force eventually become significant and larger-scale balanced flow dynamics become important or dominant. For example, Raymond and Jiang (1990) showed that potential vorticity (PV) anomalies of size and magnitude associated with those generated by MCSs can generate sufficient ascent in their inflow to initiate convection, thus helping sustain the system. Olsson and Cotton (1997) analysed nonlinear balance in a modelled mesoscale convective complex to show that the major unbalanced part of the flow is the large-scale downward vertical motion. As they point out, this is because balance does not imply no role of gravity waves, but rather instantaneous adjustment by gravity waves propagating effectively infinitely fast, so it is the longer-range influence of gravity waves for which imbalance is most important. Cotton *et al.* (2011) provide a more in-depth survey.

These conceptual models are based upon quasi-steady, or slowly evolving flows (RKW theory invokes several stages in the system life history), naturally motivated by the need to explain the existence of long-lived systems (e.g. Moncrieff and Miller, 1976). However, it is also recognised that such systems may interact with other mesoscale flows which may be particularly prevalent in coastal terrain. For example, Kingsmill (1995) describes the interaction of a

thunderstorm-generated gust front and a sea-breeze front, and its role in convective initiation and Lombardo and Colle (2012) discuss the processes determining the lifetime of linear MCSs on crossing a land/sea boundary.

In this article we describe the early stages of development of an MCS which broadly follows these quasi-steady ideas but which developed through unsteady transitions as it interacted with an evolving environment. The objectives of the article are to elucidate the observed structure of the MCS and how it changed in time, particularly focussing on a major transition period. Model simulations of the event are presented in Clark *et al.* (2013), referred to as Part 2 hereafter, to gain some insight into the processes contributing to this structure, with particular emphasis on the contribution from different microphysical processes.

The detailed nature of the MCS observed in IOP 18 changed with time but, in summary, an area of intense thunderstorms 100 km or more across could be identified in radar and satellite imagery moving eastsoutheast towards Kent, passing over Chilbolton at the centre of the CSIP area at about 1100 UTC, and eventually crossing the coast of southeast England (Kent and Sussex) at about 1345 UTC. The system re-intensified over France once it had crossed the English Channel and could be identified in satellite imagery at least until the end of the day. The detailed evolution over the UK will be discussed and illustrated with satellite and radar imagery below.

Primary initiation of the convection leading to the MCS took place outside the CSIP area and will not be the focus of this article. However, the MCS was in the early stages of development as it entered the CSIP area and its evolution was well-observed as it passed through the area. The focus of this article is the development of the MCS structure with time through the initiation of new convective cells. On time-scales of an hour or more, the system was long-lived and maintained a fairly consistent propagation velocity. However, on shorter time-scales the MCS exhibited a lot of interesting non-steadiness, with new lines of showers forming in advance of their predecessors (which travelled with the slower steering-level winds). The MCS also overtook and absorbed another line of shower clouds that formed ahead as a result of an entirely different mechanism (a coastal convergence line). As the MCS intensified by absorbing these shower lines, it produced an even bigger cold pool that triggered the development of a bow echo and trailing area of suppressed convection.

Simulations using the non-hydrostatic Met Office Unified Model at 1 km horizontal grid size, presented in Part 2, were able to reproduce well the general behaviour of the MCS and propagating cold pool. The above-mentioned details of the evolution were not so well reproduced but, nevertheless, sensitivity studies with the model provide some insight into the important processes operating during the event.

2. Observations

Browning *et al.* (2007) show the locations of the numerous observational instruments deployed in southern Britain during the campaign. The CSIP campaign was centred on the Chilbolton observatory. The main, steerable radar dish was used with the 3 GHz Chilbolton Advanced Meteorological Radar (CAMRA; Goddard *et al.*, 1994). Temporary radiosonde launch sites were set up at Reading, Bath, Swanage, Preston Farm and Chilbolton, launching

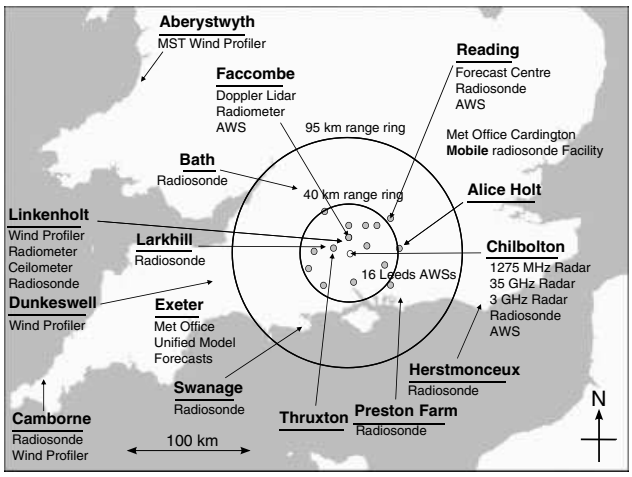

Figure 1. Location of key instrument systems.

every hour where possible. A network of automatic weather stations (AWSs) provided near-surface wind, temperature, humidity and pressure data. The locations of key systems for IOP 18 are shown in Figure 1.

A number of operational systems were also central both to the execution of the campaign and the analysis presented here. The Met Office radar network (RADARNET) provided composites of analysed surface rainfall rate (a mixture of 1, 2 and 5 km resolution) every 15 min, and surface rainfall rate data from individual radars were available every 5 min. Meteosat Second Generation (MSG) provided data every 15 min (Schmetz *et al.* (2002)), in particular the high-resolution visible channel (HRV), 'water vapour' images and derived cloud-top heights based upon IR channels. These were processed through the Met Office AUTOSAT system. The MSG HRV was supplemented by available MODIS visible images. Routine surface synoptic data were available from operational stations (SYNOPs). These are generally available hourly, but a number of stations have been augmented to provide data every 10 min. The frequency of operational radiosonde releases was increased to 3 h at Camborne and Herstmonceux, and 2 h at Larkhill.

3. Synoptic Overview

Figure 2 shows the Met Office's surface synoptic analysis at 1200 UTC on 25 August 2005. The UK was embedded in a westnorthwest geostrophic flow behind the frontal system associated with a cut-off low centred to the north of the UK (about 65°N, 5°W). The cold front had passed through the CSIP area before 0000 UTC, and the showers observed during the IOP were associated with the cold maritime flow behind the front. Figure 2 also shows the location of the MCS close to the south coast of England at this time.

Figure 3 shows observations from the Larkhill radiosonde released just ahead of the MCS at 0957 UTC. There was a distinct tropopause at about 350 hPa with a dry layer beneath ($\theta_s \sim 13\,^{\circ}$C) capping a moist layer with lower θ_s of about 10–11 °C. (θ_s is the wet-bulb potential temperature, θ_w, the air would have if saturated; if a parcel of air with given θ_w is lifted moist adiabatically to a level with given θ_s, then if $\theta_w > \theta_s$ the parcel is positively buoyant). Analysis of the radiosonde profile shows that parcels from the super-adiabatic surface layer were convectively unstable, with Convectively Available Potential Energy (CAPE) about

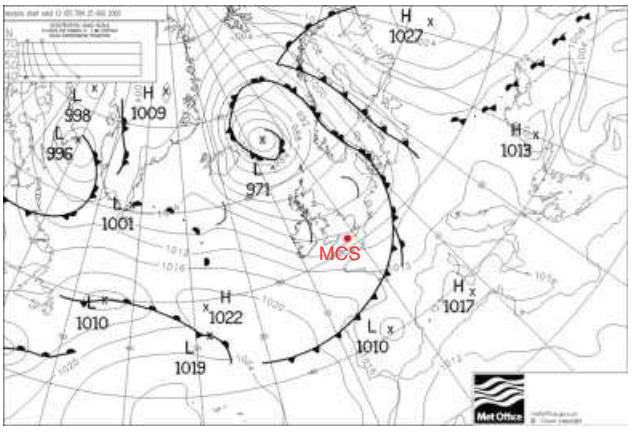

Figure 2. Met Office surface synoptic analysis at 1200 UTC on 25 August 2005. The position of the MCS at this time is shown by a dot over southern England. This figure is available in colour online at wileyonlinelibrary.com/journal/qj

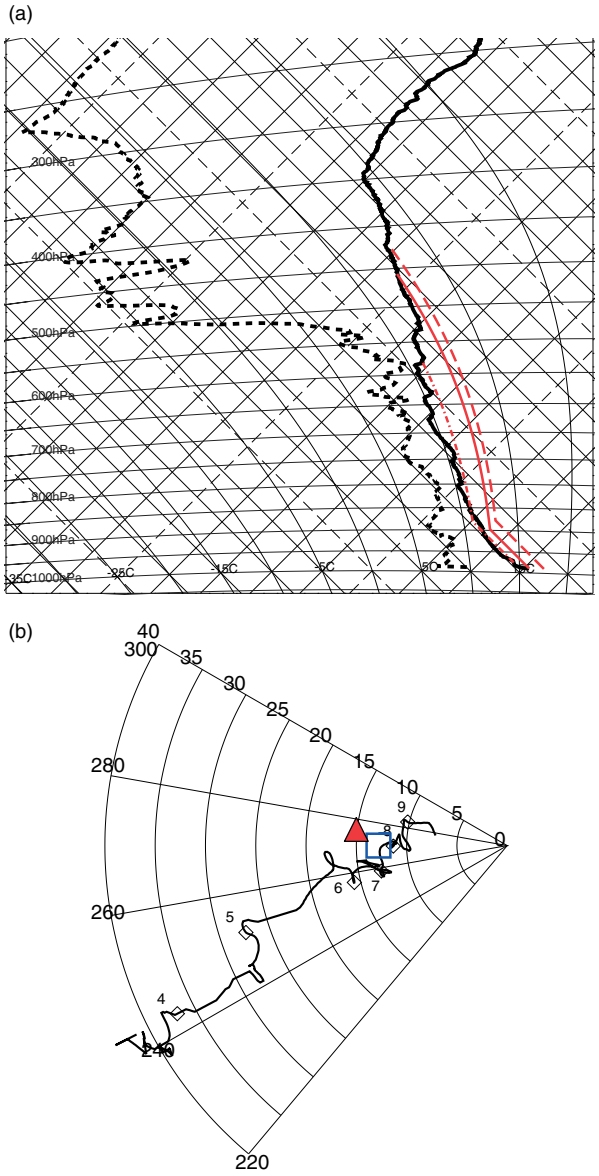

Figure 3. (a) Tephigram showing temperature (full line) and dewpoint (dashed line) profiles from radiosonde released from Larkhill at 0957 UTC on 25 August 2005. The dashed and dash-dotted lines show parcel ascents discussed in text. (b) Hodograph of wind profiles from the same profile as (a). Pressure levels are marked every 100 hPa by small numbered diamonds, labelled in hPa/100. The estimated cell velocity is indicated with a large open square, and the estimated cold pool propagation velocity with a large filled triangle. This figure is available in colour online at wileyonlinelibrary.com/journal/qj

450 J kg^{-1} (dash-triple-dot line), and equilibrium level around 450 hPa, but parcels representative of the convective boundary layer as a whole (dash-dot line) were inhibited by a weak lid at the top of the boundary layer. A more substantial lid existed at about 525 hPa, but only a little more boundary-layer heating (a degree or two in near-surface temperature) would have been needed to produce parcels able to penetrate this intermediate lid and reach the tropopause with CAPE of about 100–200 J kg^{-1}. Surface measurements shown later show that the peak screen temperature reached just ahead of the MCS was about 18 °C. With this parcel temperature at the surface (dashed line) the tropopause around 400 hPa can be reached with CAPE 630 J kg^{-1} from the observed sounding and 890 J kg^{-1} from the model. It is possible that the CAPE increased as colder air arrived aloft during the day, but unlikely that CAPE more than about 500–600 J kg^{-1} occurred. Thus, the instability was fairly modest.

The wind profile (Figure 3(b)) shows a westsouthwesterly upper-level jet. Low-level winds were veered compared with the mid-troposphere with an overall change in wind direction of 40–50° from 1 km (∼900 hPa) to 6 km (∼450 hPa). This is consistent with the horizontal temperature gradient.

The MSG water vapour image at 1200 UTC is shown in Figure 4(a). This shows the very dry (dark) region associated with the low tropopause behind the front. Dark zones such as this in water vapour imagery are known to be associated with upper-level PV maxima (Browning, 1997) corresponding to the depression of the tropopause. Convective cloud is evident over the UK and the MCS itself is evident with a relatively dark ring surrounding it and a relatively dark line through it dividing Line A from Lines C/E (see below). The water vapour image may be compared with Figure 4(b), which shows the height of the 2 pvu surface at 1200 UTC forecast by the Met Office's operational 12 km grid size model (from 0000 UTC). (1 potential vorticity unit = 10^{-6}m^{2}s^{-1}K kg^{-1}) This corresponds approximately with the dynamical tropopause (Hoskins *et al.*, 1985). Note that this is the highest height of the PV=2 surface; regions of infinite gradient correspond to folds in the surface with a second and third PV=2 surface beneath (unless the fold is vertical). The qualitative structure of the forecast tropopause agrees very well with the water vapour image. The main tropopause fold is evident running along a line to the south of the northwest coast of France. A second abrupt lowering of the tropopause is evident behind this, with a fold at 6 to 7 km running from the coast of Southeast England to the southwest of England. This high-PV region corresponds to the layer of high static stability in Figure 3, which limits the depth of convection to 7–8 km (about 400–425 hPa).

Figure 5 shows time–height cross-sections constructed from sondes launched from Larkhill and Preston Farm, over which the MCS passed. The cross-sections show wet-bulb potential temperature, θ_w, below the lifting condensation level, and the saturated wet-bulb potential temperature, θ_s, above. The radiosonde launched from Preston Farm at 1200 UTC recorded data up to only 700 hPa, probably because it was struck by lightning at the leading edge of the MCS. Both cross-sections show the arrival of a deep

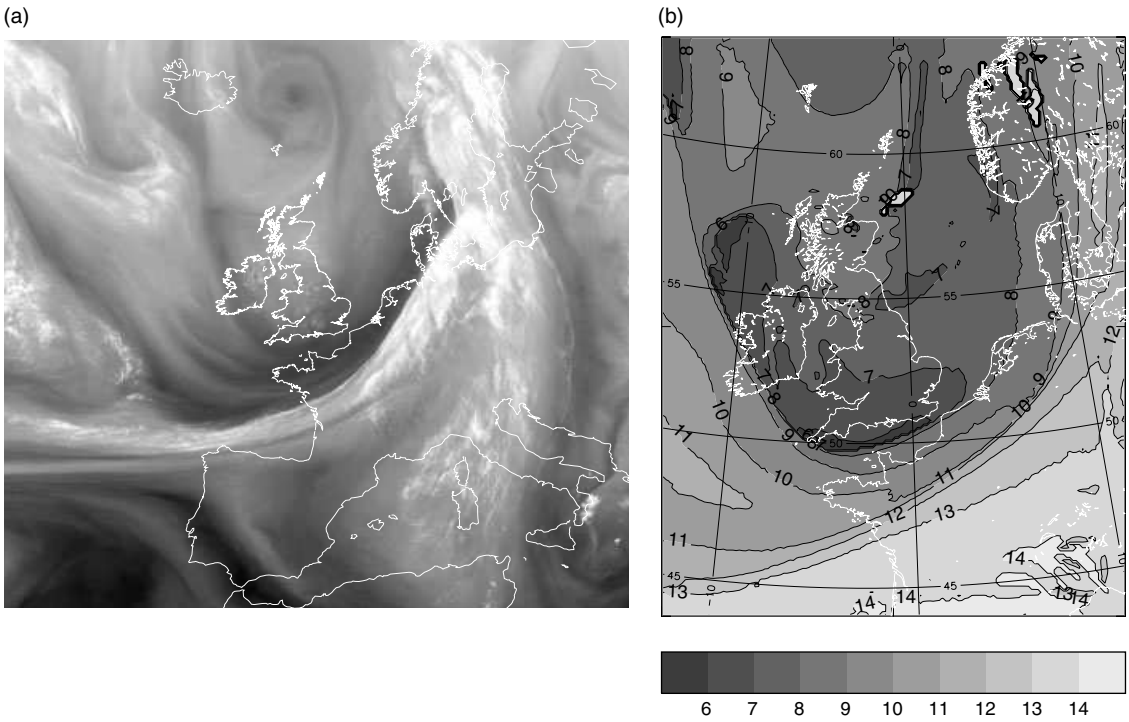

Figure 4. (a) Meteosat Second Generation water vapour image at 1200 UTC on 25 August 2005. (b) Height (km) of PV=2 pvu surface at 1200 UTC forecast from the 0000 UTC run of the operational forecast from the Met Office's 12 km model.

region of low-θ_s air, deepening up towards the tropopause as the tropopause descended. This is consistent with the structure of a cold anomaly located beneath the tropopause depression due to a PV anomaly as discussed by Bishop and Thorpe (1994).

Also shown in Figure 5 is the surface θ and θ_w (at Larkhill in Figure 5(a) and Rotherfield, the nearest AWS to Preston Farm, in Figure 5(b)). The Rotherfield data have been shifted by 25 min to account for mean system velocity between the sites. The Larkhill data show a high-θ_s (about 12 °C) lid at about 875–900 hPa which disappeared between 0800 and 1000 UTC. It is likely that this was eroded as the boundary layer warmed. At about 1000 UTC, θ_s in the lower layers of the sounding was about 10.5–11 °C. The surface θ_w was a little higher (up to 13 °C). This suggests instability at least up to 550 hPa. The Preston Farm data show that a well-mixed boundary layer developed with θ_w around 12 °C at 1100 UTC (13 °C at the surface). Convection is likely up to around 500 hPa.

In summary, the widespread convection observed corresponded to the passage of an upper-level PV anomaly and associated cold anomaly below the tropopause over relatively high-θ_w air near the surface. Initial triggering of convection became possible when an inhibiting 'lid' disappeared between 0800 and 1000 UTC.

4. Observations of a boundary-layer cold pool and associated cloud arc, bow echo

The convection which was observed in the CSIP area became an organised MCS, eventually exhibiting a distinct cloud arc and bow echo in satellite and radar imagery. This section presents an overview of observations of the cold pool associated with the MCS, derives estimates of the overall mean system velocity based upon the cold pool, and presents observations of the cloud arc and bow echo.

Both radiosonde cross-sections in Figure 5 show the presence of a cold pool in the boundary layer in the form of depressed θ_w (down to 9 °C at Larkhill, 10 °C at Preston Farm).The detail in the cross-section is unreliable, as the cold pool is poorly sampled in time, but the surface θ and θ_w show the extent of the cold pool at the surface. The surface cold pool at Larkhill has fairly complex structure, with several dips in temperature. That at Preston Farm is very distinct and lasts at least 1.5 h. A gradual recovery is also evident as surface heating warmed the cold pool and a new boundary layer grew. This is shown particularly well by the more frequent sondes at Preston Farm.

The substantial surface cold pool was also evident in many other near-surface temperature measurements, examples of which will be discussed in more detail later. This cold pool was generated by the MCS, the development and sub-structure of which will be discussed further below. Table 1 summarises the observations made using the AWS and SYNOP sites. In each case, two times are given for the passage of the cold pool, corresponding to the time of quickest decrease in temperature and the time of the end of decrease (i.e. the minimum) in temperature. In the case of the AWS data, these have been derived from data smoothed with a 10-point (30 s) running mean to remove high-frequency noise. The temperature change and pressure change are also given. The peak pressure rise is not always coincident with the peak temperature drop. In some cases (e.g. Thruxton) a larger pressure rise is seen about one hour later, associated with a smaller temperature drop. (This corresponds to Line A – see later). Other columns in Table 1 will be discussed below.

The AWS data and 10 min Met Office data in Table 1 have been used to estimate the overall propagation speed of the cold pool. Later, in sections 5 and 7.2, we discuss the use of the pressure drop (Δp) to estimate propagation velocity (v_p) from single-site data. In this section, however,

Table 1. A summary of the time of passage of the gust front over the various CSIP AWSs (two-digit site id) and Met Office SYNOP sites (four-digit site id). Sites are ordered by the time of passage of minimum temperature. See text for further explanation. Values of propagation velocity, v_p, have been derived from the pressure change as explained in section 5.

Site id	Site name	Site letter	Time of max $-\partial\theta/\partial t$	Time of min θ	$\Delta\theta$ (°C)	Δp (hPa)	v_p (m s^{-1})	Associated Line
16	Wilton House	E	1033	1050	6.7	0.7	10.8	B
11	Larkhill	T	1022	1058	4.2	0.6	10.0	B
3743	Larkhill	T	1020	1100	4.2	0.7	10.8	B
3746	Boscombe Down	B	1030	1100	4.9	0.9	12.2	B
12	Thruxton	F	1045	1104	4.0	0.6	10.0	B
09	Woodlands Farm	M	1109	1112	3.8	0.5	9.1	B
10	Silchester	R	1109	1120	4.5	1.0	12.9	B
3749	Middle Wallop	W	1030	1120	4.6	0.8	11.5	B(/C)
26	Chilbolton	C	1054	1121	6.5	0.9	12.2	C
22	Lyburn	P	1046	1131	6.8	1.4	15.3	C
23	Chilworth	D	1108	1137	7.6	1.7	16.8	C
3862	Hurn	H	1110	1140	4.5	1.1	13.5	B(/C)
14	Stoken Farm	N	1103	1142	4.9	1.1	13.5	B
20	Rotherfield	Q	1139	1225	6.9	1.6	16.3	C
3761	Odiham	O	1140	1230	4.9	1.3	14.7	B
3769	Charlwood	A	1240	1310	7.2	1.8	17.3	E
3882	Herstmonceux	X	1250	1340	7.6	1.7	16.8	E

we shall derive the average propagation velocity from the field of surface stations using the times of arrival of the temperature drop. Two times have been used: the time of maximum cooling rate (taken as close to the leading edge) and the time of minimum temperature. The latter is typically 20–40 min later than the former. Linear regression of longitude against the time of maximum cooling rate (not shown) gives a west–east speed of 15.0 m s^{-1} between 1020 and 1350 UTC ($r^2 = 0.89$). Almost all points lie sufficiently close to the best line on the longitude plot to give confidence that the sites experienced the passage of the same cold pool, but there is sufficient scatter that variations of a few m s^{-1} would remain consistent with this fit, as would a somewhat nonlinear curve. The latitude plot is much more scattered. To some extent this reflects the initial orientation of the gust front (stations further south see it later) but it is also affected by the southward component of propagation. The best-fit line gives a south–north speed of -1.6 m s^{-1}, but this is very uncertain. The resulting propagation velocity (15.1 m s^{-1} in a direction from 276°) is marked on the hodographs in Figure 3(b). This velocity is much faster than the near-surface wind ahead of the cold pool. It is close to the observed wind around 700 hPa but veered by about 15–20°. It will be shown below that a single propagation speed is not appropriate, but this estimate provides a useful reference for the system as a whole.

A regression has also been applied using the time of minimum temperature. The resulting propagation speed is somewhat slower, at 13.1 m s^{-1} west–east, and -2.0 m s^{-1} south–north, i.e. 13.2 m s^{-1} from 278°. It is evident that the temperature minimum becomes less sharp with time and the cold pool grows in extent both along and across its direction of travel. The combination of these two estimates results in the choice of 14 m s^{-1} used below in the construction of Figure 9(a).

The surface cold pool arrived at Preston Farm shortly after 1200 UTC. By this time the MCS had reached a mature stage. Figure 6(a) shows an MSG visible image at 1230 UTC; the MCS is evident as a large mass of cloud with a clear region behind (i.e. to the west and northwest of it) which is presumably due to the rear of the cold pool suppressing convection. Cloud-top products from MSG IR channels (not shown) show the top of this cloud mass reaching generally between 6 and 7 km, with a few peaks between 7 and 8 km.

From 1230 UTC until about 1430 UTC, the northern half of the MCS remained over land and continued to produce intense rainfall (associated with frequent lightning according to spherics data, Lee, 1990) and also produced higher cloud tops (some above 9 km). By this time, land temperatures, near the surface, were exceeding 18–19 °C ahead of the cold pool. The southern half of the system, however, travelled over the sea. According to the operational analysis, the sea-surface temperature was about 16.6 °C near the south coast and somewhat higher (17–17.5 °C) further east in the narrowest part of the English Channel. The cooler boundary-layer inflow air reduced convective activity very rapidly, with the result that the head of the gust front at the leading edge of the cold pool was defined by a thin rope cloud, i.e. a line of small, relatively shallow, convective clouds, with individual elongated anvils each extending from individual cloud cells towards the north or northnorthwest (Figures 6(b, c)). The orientation of the cells is explainable in terms of the ex-boundary-layer air within the anvils travelling due east whereas the triggering points for new ascent (the rope cloud) advanced broadly eastwards but with a component from the north. The central section of the rope cloud (mainly associated with precipitation) is identified as Line E below, but it clearly extends further west as less intense clouds and with a more irreglar shape, and further northeast at the other end, becoming indistinct as the cloud deepens and shows more cirrus over land.

Figure 6(d) shows a bow echo in network radar data associated with the cloud arc in Figure 6(c) approaching the French coast with moderately intense rain along it at 1430 UTC. Cloud-top heights associated with the bow echo over the sea were only about 3–4 km (with one small cell reaching 5 km). As already noted, this shallower convection produced much smaller anvils than the deeper convection associated with parts of the MCS over land and so the gust front (rope cloud) is visible in MSG HRV imagery very clearly. Figures 6(c, d) also show that the (still precipitating) cirrus shield from the remnants of the MCS had separated

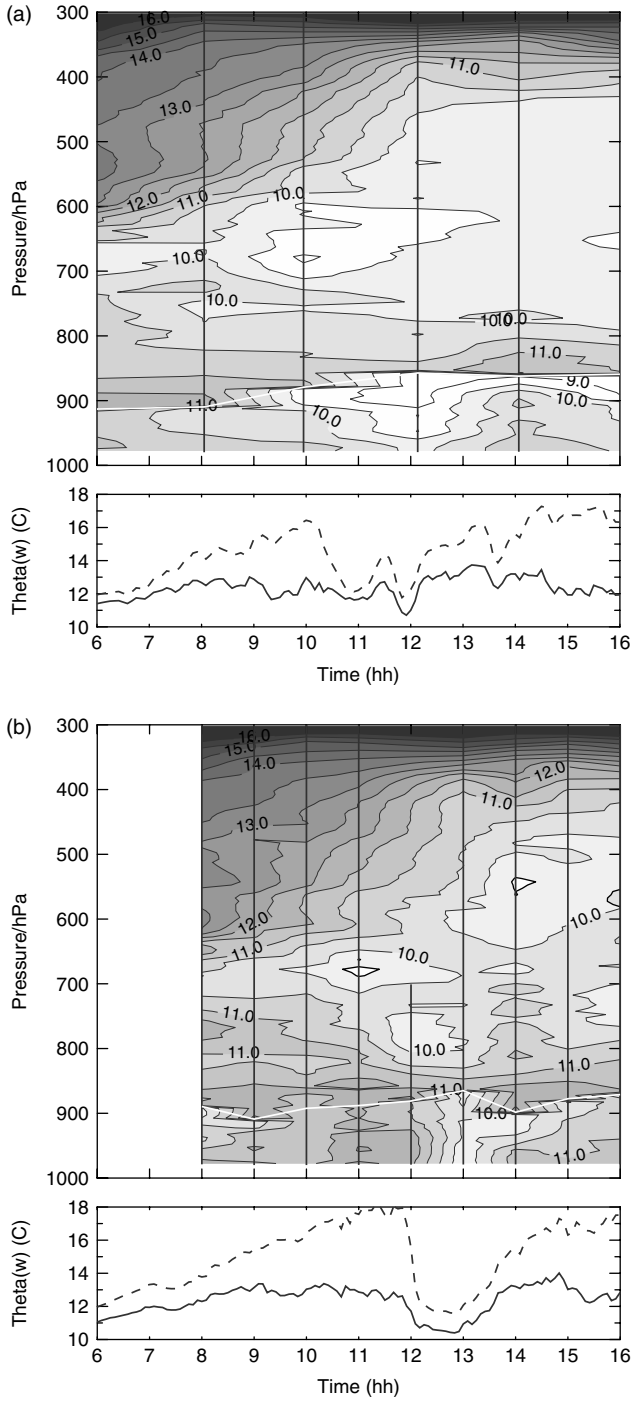

Figure 5. Time–pressure cross-sections constructed from radiosonde data and surface θ (dashed) and θ_w (solid) plotted beneath: (a) Larkhill (51°12′N, 1°48′W), (b) Preston Farm (50°53′N, 0°47′W). (Surface from Rotherfield displaced 25 min later – see text). The solid white line indicates the lifting condensation level (LCL) from the radiosonde profile assuming a parcel derived from the 1000–950 hPa layer. θ_w is plotted below the LCL, and θ_s above it (both in °C). The vertical black lines indicate the launch times and pressure range of the radiosondes used to construct the figures.

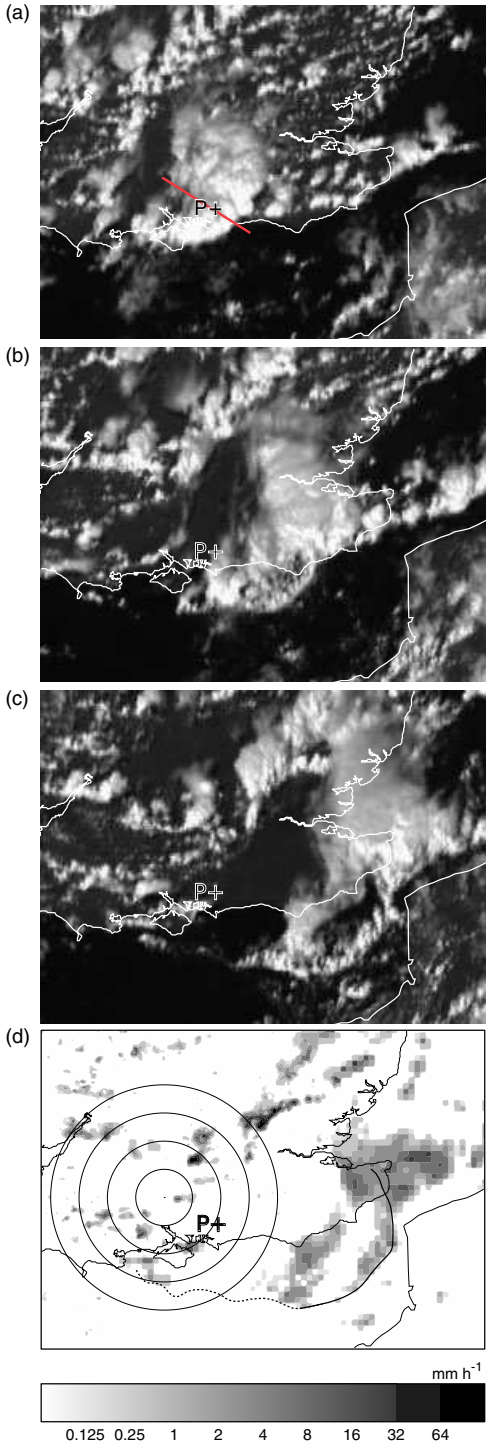

Figure 6. MSG High-Resolution Visible images at (a) 1230 UTC, (b) 1330 UTC and (c) 1430 UTC on 25 August 2005. (d) shows network radar rainfall rates (composite of 1, 2 and 5 km products) at 1430 UTC. Range circles are at 25 km intervals centred on Chilbolton. The line in (a) shows the position of the RHI scan shown in Figure 7. The solid/dashed line in (d) shows the leading edge of the rope cloud shown in (c), with the solid segment identified as Line E. The cross labelled 'P' marks Preston Farm. This figure is available in colour online at wileyonlinelibrary.com/journal/qj

from the cloud arc and was drifting towards the east (reaching a height of about 5–6 km).

Figures 6(c, d) show the main MCS to be travelling away from the extreme southeast of England but it is also of interest to note the very intense line of rain north of London. This was a recent intensification of part of a line of showers similar to the system under study which originated over the coast of northern England and North Wales. It would appear from the satellite and radar imagery that the intensification occurred as this line encountered the trailing northern boundary of the cold pool associated with the overall MCS being studied here, though we have no additional data to verify this. Prior to this intensification, there was no clear indication of the trailing edge of the cold pool on cloud or rainfall imagery.

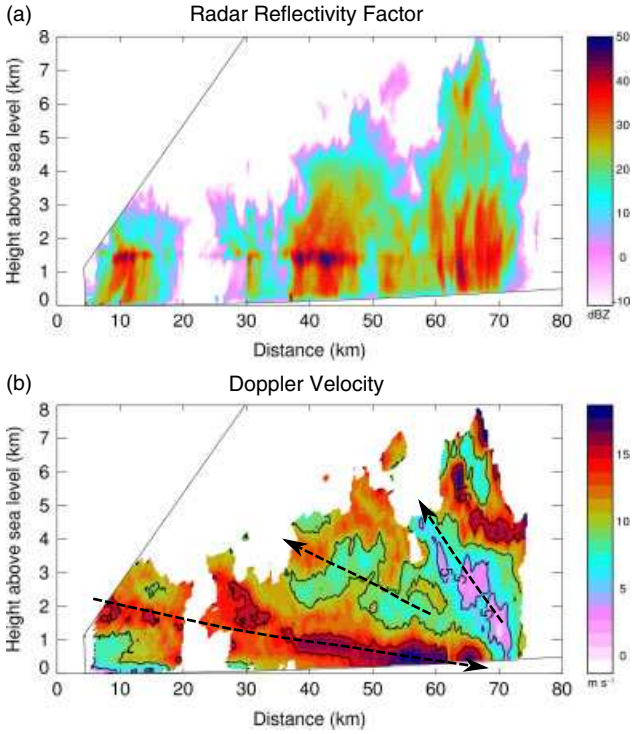

Figure 7. RHI from Chilbolton CAMRA radar at 1228 UTC, 120° azimuth: (a) radar reflectivity factor, and (b) radial Doppler velocity ($m\,s^{-1}$, positive away from the radar). System-relative flow is shown schematically by the black dashed arrows. This figure is available in colour online at wileyonlinelibrary.com/journal/qj

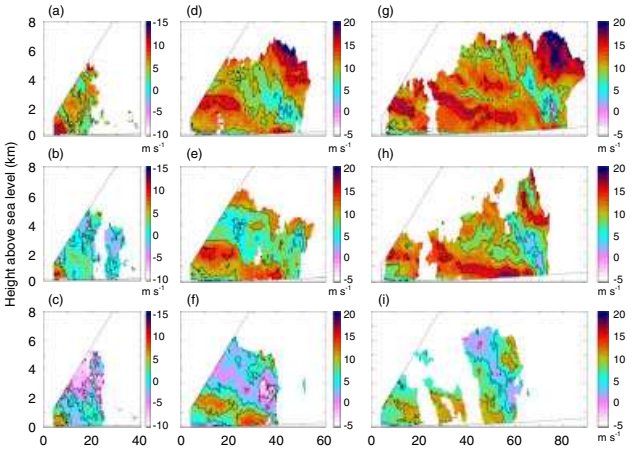

Figure 8. RHI scans of Doppler radial velocity from Chilbolton CAMRA radar at: (a) 1107 UTC, 143° azimuth, (b) 1105 UTC, 168° azimuth, (c) 1103 UTC, 189° azimuth, (d) 1150 UTC, 100° azimuth, (e) 1148 UTC, 120° azimuth, (f) 1146 UTC, 143° azimuth, (g) 1229 UTC, 100° azimuth, (h) 1228 UTC, 120° azimuth, and (i) 1226 UTC, 143° azimuth. The positions of the scans in (a, b, c) are shown on Figures 9(b) and 14(c). The positions of the scans in (d, e, f) are shown on Figure 14(f). The positions of the scans in (g, h, i) are shown on Figure 12(f). This figure is available in colour online at wileyonlinelibrary.com/journal/qj

The vertical structure of the mature MCS was observed in a number of RHI scans from the CAMRA radar. Figure 7 shows the RHI at 1228 UTC, 120° azimuth, which is close to perpendicular to the cloud arc shown in Figure 6(a). It shows a very large precipitation region between about 30 and 75 km from Chilbolton. This region has two sub-regions of deeper reflectivity. One was centred at 50 km and reached an altitude of about 5.5 km (identified as Line B below). The other was centred at 67 km, corresponding to the leading edge of the MCS (Line E below), and reached an altitude of about 7.5 km. The vestiges of another convective line (Line A) are visible between 5 and 15 km, reaching an altitude of only about 3 km. No radar scans (or other data) show evidence of substantial elevated convection.

The radial Doppler velocity in Figure 7(b) shows a low-level jet, probably continuous (long lowest dashed arrow) within the RHI out to the gust front at a range of 65–70 km. The strongest flow (which peaks at $18.4\,m\,s^{-1}$) is below about 1 km between 40 and 70 km from Chilbolton and corresponds with the cold pool. The low-level jet slants downwards, with its axis descending from 2 km to below 1 km at 40 km and beyond. This flow is deeper and slightly less strong further behind the front. It probably corresponds to a rear-inflow jet as described by Weisman (1992) and analysed more fully by Pandya and Durran (1996). Note that the Doppler data are only available where significant reflectivity is present. As a result, the origin of the low-level jet is indistinct and may be complicated by the presence of a second band of rain. Model simulations described in Part 2 show this jet originating at about 4 km at the rear of the system.

A slanting slow layer is apparent above this between 60 and 70 km (top dashed arrow); it appears to originate at the leading edge of the precipitation and probably corresponds to updraught air originating in the boundary layer ahead of the MCS which travels rearwards relative to the advancing storm. An intermediate layer of low-velocity air lies above the low-level jet (middle dashed arrow), perhaps associated with slow rearward slantwise ascent originating at the leading edge of another part of the MCS. The layers of slantwise convection evidently coexist with, and feed, the plumes of upright convection which were responsible for the higher tops discussed previously. It is difficult to precisely estimate the vertical velocities associated with this slantwise convection, but assuming a $12\,m\,s^{-1}$ system speed along the cross-section suggests an updraught around $0.4\,m\,s^{-1}$ and downdraught about half this (perhaps up to $-0.25\,m\,s^{-1}$). This may be compared with the updraught corresponding to the top dashed arrow, which is an order of magnitude stronger, about $3–5\,m\,s^{-1}$. Note that we have no direct measure of the origin of the mid-level rearward slantwise ascending air; in Part 2 we confirm that back-trajectories show that at least some of this air in model simulations originates from slantwise ascending air at mid-levels ahead of the system. Unfortunately the radiosonde released just ahead of the system did not survive to sufficient height to provide any direct evidence of inflow ahead of the system.

Similar features are apparent in scans at azimuths 100°, 120° and 143° between 1146 and 1150 UTC and again between 1225 and 1229 UTC (Figures 8(d)–(i)). Though there is clearly some development in time, there is consistent progression in structure moving from southwest (Figure 8(c, f, i)) to the northeast (Figures 8(a, d, g)), with strengthening stantwise flows and more evidence of stratiform precipitation. As will be become evident below, the overall system development broadly resembles the parallel-stratiform systems studied by Parker (2007a,b). The progression in Figure 8 is essentially down-shear, and the structure is similar to the control system of Parker (2007a) in its later parallel stratiform/trailing stratiform transition. The system propagation relative to the mid-level flow essentially represents the development of this structure

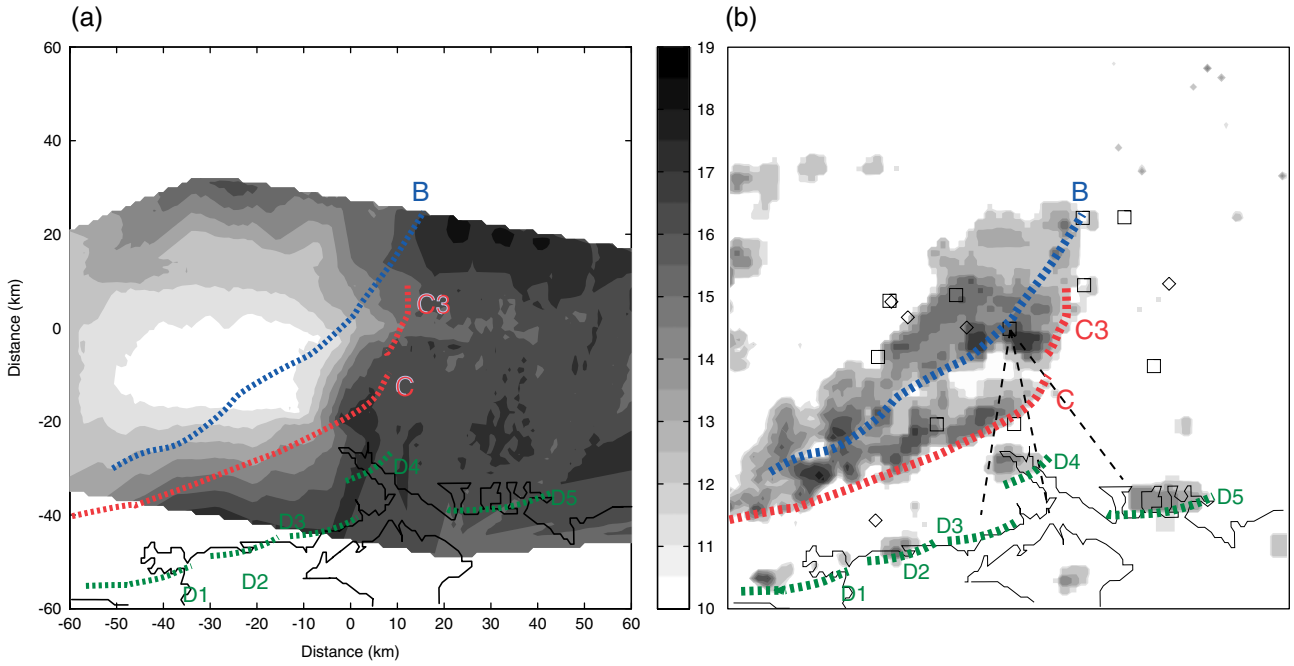

Figure 9. (a) Analysis of surface potential temperature (°C) at 1100 UTC on 25 August 2005, showing the cooling associated with the cold pool. (b) Network radar rainfall rates (composite of 1, 2 and 5 km products; note transition to 5 km data near coastal area) at 1100 UTC. The grey scale is logarithmic as in Figure 6(d), and peak rates are greater than 32 mm h^{-1}. Also marked in (b) are locations of AWS (squares) and 10 min SYNOP stations (diamonds) used to derive (a). The grey dotted lines in (a) and (b) show analysed leading edges of convection. Lines B, C and D are derived from radar and MSG satellite imagery (section 6 gives discussion of these lines). The straight dashed lines in (b) show positions of RHI scans in Figure 8(a–c). This figure is available in colour online at wileyonlinelibrary.com/journal/qj

roughly perpendicular to the shear vector and initial line orientation.

Comparison of pairs of scans along the 100° azimuth separated by 40 min results in an estimated propagation speed along the scan of 13.7 m s^{-1} (with an uncertainty of about 1 m s^{-1}). That along the 120° is 10.4 m s^{-1}. Note that the component of the largest mean system velocity based on the leading edge of the surface cold pool discussed above along the 120° azimuth is a little faster than this at 13.8 m s^{-1} but with similar uncertainty. By chance, during this period the leading edge of the MCS aligns quite closely with arcs centred on Chilbolton, so the radial propagation speed corresponds quite closely with the actual radial propagation speed of the system, though there is undoubtedly a significant component of flow perpendicular to the RHI scans. Comparison of the CAMRA Doppler signal peak radial wind speeds in the low-level jet (reaching over 18 m s^{-1} along the 120° azimuth) with the propagation speed (10.4 m s^{-1}) indicates substantial relative flow towards the gust front. Air in upper and lower low-velocity layers, believed to be associated with sloping updraughts feeding the MCS, was travelling rearwards relative to the system at over 7 and 2 m s^{-1}, respectively. This was fed by relative flow near the surface that was towards the gust front from the front side as well as from the rear.

Figure 9(a) shows the surface cold pool at 1100 UTC based on an analysis of the near-surface temperature from the 17 surface stations whose positions are plotted in Figure 1. A number of assumptions have been made to derive this. In particular, it has been assumed that the time series at a site (between 1000 and 1200 UTC) can be translated into a series of data along a line assuming a translation speed of 14 m s^{-1} from 280°, corresponding to the average propagation speed over the whole domain derived above. This is slightly faster than the speed derived along the radar RHI. Some of the discrepancy may be due to the radar RHI not being perfectly aligned with the propagation direction, and some due to the unsteady nature of the propagation to be discussed below. However, the discrepancy is not sufficient to have major impact on the conclusions drawn below.

The rainfall distribution at 1100 UTC from the parent storms generating the cold pool is shown in Figure 9(b). The cold pool covers a wide area (around 60 km across), with the MCS rainfall lying on its southeastern flank. The near-surface temperature perturbation is substantial, up to 6 or 7 K. The shape of the perimeter of the cold pool may be, to some extent, an artefact of the analysis technique. Data are sparse, especially to the south, and there are gaps in the surface data along the rain band. However, it is clear that the leading edge of the cold pool corresponds broadly with the leading edge of the precipitation. A number of lines are shown in grey; these correspond to the leading edges of individual precipitation lines within the MCS. The detailed evolution of these lines will be discussed in sections 6 and 7.

To summarise this section, observations have demonstrated the existence of a large surface cold pool beneath an extensive region of precipitation with at least 6–7 K temperature perturbation behind the leading edge of the MCS. Table 2 shows a summary of the various speeds derived in this section and later. A measure of the overall system velocity based on near-surface measurements of the cold pool confirms that the measurements were affected by a single system propagating at an average speed of upto about 15 m s^{-1} from a few degrees north of west, though some variation with time is likely. This is similar to, but veered 15–20° from, the wind speed ahead of the system at about 700 hPa, close to the middle of the unstable layer. The leading edge of the cold pool corresponded to a low-level jet (and gust front) with maximum winds 5–6 m s^{-1} faster than the system propagation speed. The low-level jet appears to have

Table 2. A summary of the various propagation and wind speeds.

Method	Speed ($m\,s^{-1}$)	Direction (deg)
Cell speed	12.8	270±5
Cold pool leading edge (mean 1020–1350 UTC)	15.1	276
Minimum temperature (mean 1020–1350 UTC)	13.2	278
Radial Doppler at 1228 UTC	18.4	300
Line-normal propagation along azimuth 120°	10.8	300
Cold-pool propagation from Eq. (4)	17	280–285

been fed by a downward-sloping rear-inflow jet from at least 65 km behind the gust front. Above this were rearward sloping updraught regions. In its later stages, the leading edge of the cold pool and associated gust front was also associated with a cloud arc (in satellite imagery) and bow echo (in network radar), in particular as the system propagated over the English Channel.

5. Propagation velocity of the gust front compared with density current theory

In this section we compare the observed propagation speed of the cold pool with estimates derived from theories of density current propagation.

5.1. Theoretical density current propagation speed

The vertically averaged ρ or θ_v deficit can be used to predict a density current propagation speed from an integral form of the classical relationship (e.g. Benjamin, 1968; Simpson, 1987):

$$v_p = \left(2g\int \frac{\Delta\rho}{\overline{\rho}}\,\mathrm{d}h\right)^{\frac{1}{2}} \quad (1)$$

$$= \left(-2g\int \frac{\Delta\theta_v}{\overline{\theta_v}}\,\mathrm{d}h\right)^{\frac{1}{2}} \quad (2)$$

$$= \left(2\,\frac{\Delta p}{\overline{\rho}}\right)^{\frac{1}{2}}, \quad (3)$$

where the integral is taken over the depth of the cold layer and the third form assumes the surface-pressure increase (Δp) is hydrostatic. $\Delta\rho$ is the density difference between the density current and its environment, $\overline{\rho}$ the average density, $\Delta\theta_v$ and $\overline{\theta_v}$ are the equivalent virtual potential temperature difference and average, g is the acceleration due to gravity and h the height.

Various theoretical, measurement and modelling studies suggest that this estimate may be too high. Droegemeier *et al.* (1987), reviewed the existing literature and performed numerical experiments. These consistently showed slower propagation speeds. Bryan *et al.* (2008) developed analytic results for a deep, anelastic, atmosphere, with limiting behaviour in agreement with Eq. (1) but generally, for cold pools of significant depth compared with the scale height of the atmosphere or the depth of the channel, the speed is slower by tens of percent.

These studies are for a stationary ambient flow, so we must also consider the momentum of the background flow in which this is embedded. Parker (1996) discussed the impact of ambient flow and shear on cold pool propagation. He showed that it is the wind strength at head-height (here perhaps 1 km) which has greatest impact and suggested a propagation speed given by

$$v_p = k_1\left(\frac{\Delta p}{\overline{\rho}}\right)^{\frac{1}{2}} - b_s U_0(H), \quad (4)$$

with empirical constants $k_1 \approx 1.2$ and $b_s \approx 0.65$, and $U_0(H)$ the ambient wind speed at the height of the top of the density current (behind the elevated nose). The constant k_1 corresponds to (but is less than) the $\sqrt{2}$ in Eqs. (1)–(3). Similar relationships are given by Liu and Moncrieff (1996), and references therein, but with somewhat smaller value for k_1 and larger for b_s.

5.2. Estimate of propagation velocity from temperature profile

Only two soundings clearly went through the cold pool, the 1208 UTC Larkhill ascent and the 1300 UTC Preston Farm ascent. Both were located roughly 50 km behind the leading edge of the cold pool. The later 1300 UTC profile at Preston Farm (Figure 10(b)) is the easier to interpret as it may be compared directly with the 1200 UTC Preston Farm ascent which was representative of the environment immediately ahead of the MCS. The pair of profiles in Figure 10(b) show cooling with a double structure: nearly −4 to −5 °C in the lowest 25 hPa and about −1.5 °C from 25 to 130 hPa above the surface. The existence of this double structure may reflect some turbulent mixing in a layer above the 25 hPa deep cold pool.

The Larkhill 1208 UTC ascent also shows the cold pool (Figure 10(a)) but, when compared with the 0957 UTC ascent from the same place, it shows cooling of about −3 °C extending only 40–50 hPa above the surface (to about 950 hPa). However, the 1208 UTC profile is actually very similar to the 1300 UTC Preston Farm profile, while the 0957 UTC profile shows an unstable boundary layer only up to about 50 hPa above the surface, compared with 150–200 hPa in the Preston Farm 1200 UTC profile. Thus, considerable diurnal heating of the boundary layer ahead of the cold pool would have happened between 0957 and 1208 UTC, so the cooling due to the cold pool may have been rather more than this comparison would suggest. It may be more useful to compare with the 1200 UTC Preston Farm ascent on the assumption that the boundary layer prior to convection would have been fairly uniform over land.

At Larkhill, Eq. (2) produces speeds of 6.9 $m\,s^{-1}$ (using the 0957 Larkhill ascent as reference) or 12.2 $m\,s^{-1}$ (using the preferred 1200 UTC Preston Farm ascent as reference). At Preston Farm it produces a speed of 12.3 $m\,s^{-1}$. The corresponding average temperature deficits are 1.4 °C over 500 m, 1.83 °C over 1200 m and 1.84 °C over 1200 m. Taking account of ambient wind and a smaller k_1 using Eq. (4), with $U_0(H) = 10\,m\,s^{-1}$ from about 280–285 (roughly the wind at 1 km), the radiosonde data result in a maximum propagation speed of about 17 $m\,s^{-1}$ from about 280–285°.

It should be noted that the average temperature deficits estimated over the depth of the cold pool (1.4 °C over 500 m or about 1.8 °C over 1200 m) are much smaller than

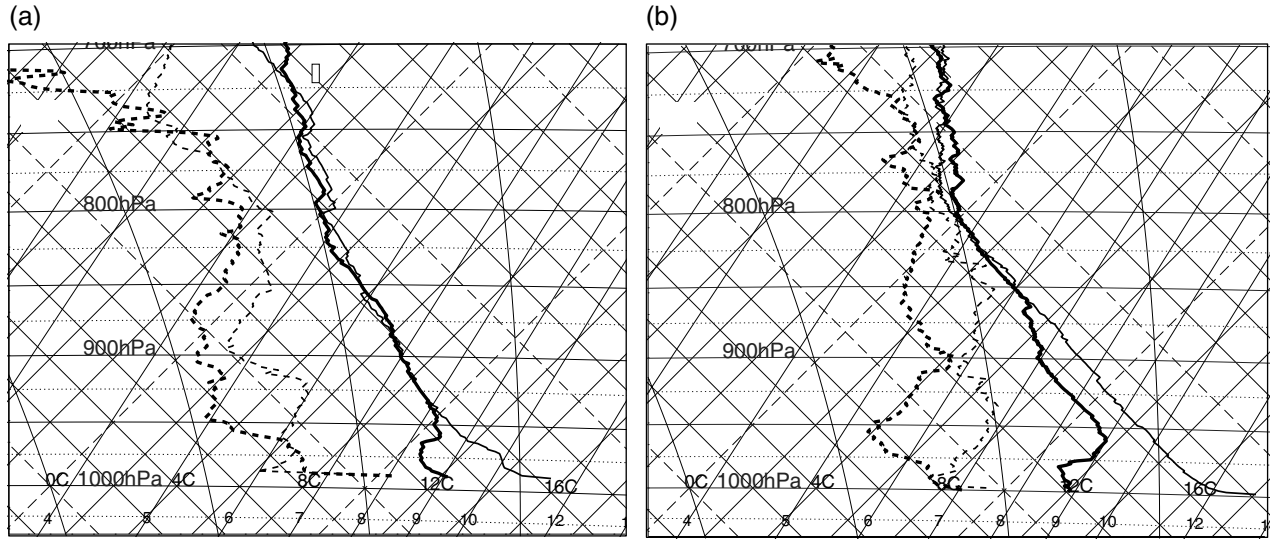

Figure 10. Tephigrams showing temperature (full line) and dewpoint (dashed line) profiles before (fine) and after (bold) passage of the gust front: (a) Larkhill launched at 0957 and 1208 UTC, (b) Preston Farm launched at 1200 and 1300 UTC.

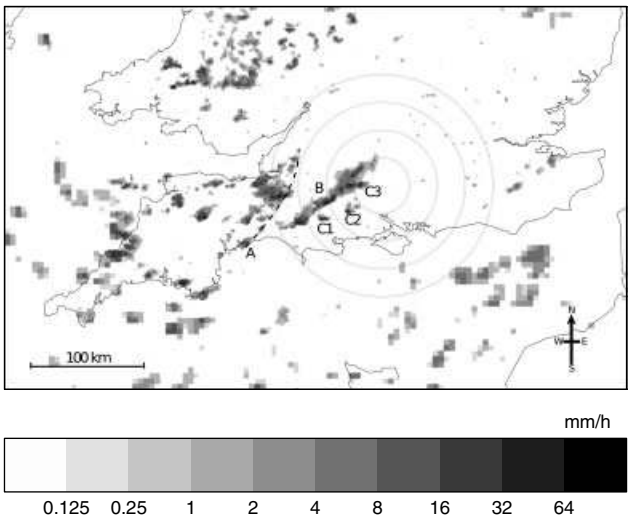

Figure 11. Network radar rainfall rates (composite of 1, 2 and 5 km products) at 1030 UTC on 25 August 2005. Circles denote ranges at 25 km intervals centred on Chilbolton. The convection Lines A (dashed) and B are marked, together with three cells (C1, C2 and C3) which go on to form Line C.

the observed near-surface temperature deficits, up to 7 °C shown in Table 1. This is partly due to the shallow nature of the super-adiabatic surface layer ahead of the storm.

5.3. *Estimate of propagation velocity from surface pressure increase*

An estimate of the propagation speed of the cold pool may also be made from the pressure increase associated with the cold pool observed in surface measurements listed in Table 1, on the assumption that this is hydrostatic. Using Eq. (3), which does not include the effect of ambient flow, the results are shown in Table 1. They clearly show considerable variability. Some variability undoubtedly arises from the difficulty of estimating the pressure perturbation (at best accurate to about 0.2 hPa), but there is also a trend with time which will be discussed further in section 7.2. Considering only those stations at which the gust front arrived between 1100 and 1200 UTC yields a mean propagation speed of 13.8 m s^{-1}, somewhat faster than the equivalent estimated from radiosondes (12.3 m s^{-1} at Preston Farm), which probably reflects the fact that the radiosondes did not sample the peak pressure perturbation. Adding the effect of ambient flow using Eq. (4) (with the same ambient flow as above) produces a speed of 18.2 m s^{-1} (compared with 17 m s^{-1} from the radiosonde).

5.4. *Comparison with observed propagation velocity*

These estimates of propagation speed may be compared with various speeds discussed in section 4: the average speeds of the leading edge and minimum temperature of the cold pool (by regression), 15.1 m s^{-1} and 13.2 m s^{-1} respectively and the propagation speed of the gust front along Chilbolton RHI scans (13.7 m s^{-1} along the 100° azimuth, 10.4 m s^{-1} along the 120° azimuth). Ignoring the ambient speed and deviations from $k_1 = \sqrt{2}$ leads to estimates lower than, though close to, the observed speeds. Taking these into account leads to estimates significantly higher than the observed speeds. While there is uncertainty in the empirical constants in Eq. (4), it seems likely that this overestimate also arises from the choice of ambient wind speed. With $U_0(H) = -10$ m s^{-1}, Eq. (4) adds 6.5 m s^{-1} to the buoyancy-driven speed; choice of a reference height closer to the surface (perhaps 300 m) could remove much of the discrepancy.

5.5. *Summary of cold pool propagation speed*

To summarise this section, the mean system propagation speed estimated above is not inconsistent with, though perhaps a little higher than, the propagation speed of the cold pool estimated from radiosonde ascents, though these ascents are of order 50 km behind the leading edge. It is also similar to, though weaker than, the flow observed in the low-level jet at 500 m above ground level at the gust front. It is also similar to that estimated from surface pressure perturbations, though there is more variability in these estimates. It is evident, therefore, that the cold-pool density current propagation speed is similar to the system

speed which is similar to the ambient wind at mid-levels. However, the matching is not perfect, and depends upon the account taken of ambient flow in estimating the propagation speed. In addition, there is evidence for both unsteadiness in propagation and significant low-level system-relative flow towards the leading edge of the system.

6. Convective substructure of the MCS

Radar and satellite imagery showed that a few light showers developed early in the day in the airmass behind the cold front, mainly triggered over the sea, though perhaps with some influence of southern Ireland later in the morning. These moved across the Irish Sea and Western Approaches towards the Bristol Channel. However, they appear to have been fairly shallow and died out on reaching land. The main shower activity was triggered over land in Great Britain. At about 0715 UTC new cells formed over Cornwall. These eventually advected towards the eastsoutheast across Cornwall but dissipated over the English Channel by about 1015 UTC. At 0730 UTC a line of showers initiated roughly along the northwest coast of Southwest England (North Devon). Satellite imagery suggests that these may have developed from pre-existing, weak showers advected in from the sea, but whether new cells or intensification of existing ones, they rapidly formed into substantially more intense showers. By 0930 these had formed into a very distinct line of thunderstorms oriented southwest–northeast and situated on the western edge of the CSIP area. This line subsequently moved through the CSIP area and, along with other developing lines, gave rise to the MCS that is the main subject of this study.

The overall MCS lasted for at least 16 h of which around 5 h were spent over southern England moving across the CSIP study area. The description in this section covers this reduced period. For the most part, individual cells in the MCS moved relative to the system – tracking a sample of six cells in the operational radar data over periods ranging from 30 to 90 min yields an average speed of 12.8 m s^{-1} towards a direction within a few degrees of east, with a general tendency to move a little north of east. This is marked on the 0957 UTC Larkhill hodograph (Figure 3(b)), and is broadly consistent with the wind in the layer around 850 hPa. However, as it moved east, the MCS as a whole propagated towards the south through the triggering of new cells. Detailed examination of the available data reveals that a number of lines of convection were involved in this process.

The composite from the radar network at 1030 UTC (Figure 11) shows two lines of cells associated with the MCS. A broken line, Line A, runs from a point roughly 80 km west of Chilbolton to the south coast. A second much more continuous line, Line B, runs from 15–30 km west of Chilbolton towards the south coast along a line oriented at about 230–050° from north. This represents Line B at its most nearly straight (2D) stage. This is the line that had intensified close to the North Devon coast around 0730 UTC. Note that the orientation of the line corresponds well (within 5°) to the wind shear vector above the cell 'steering level' wind around 850 hPa (Figure 3(b)), so clouds above this level will have tended to advect along the line. The thermal wind equation suggests, therefore, that the initial line is perpendicular to the mid-level temperature gradient. Ahead of this line in Figure 11 are two new cells (labelled C1 and C2) which went on to form part of Line C, and the

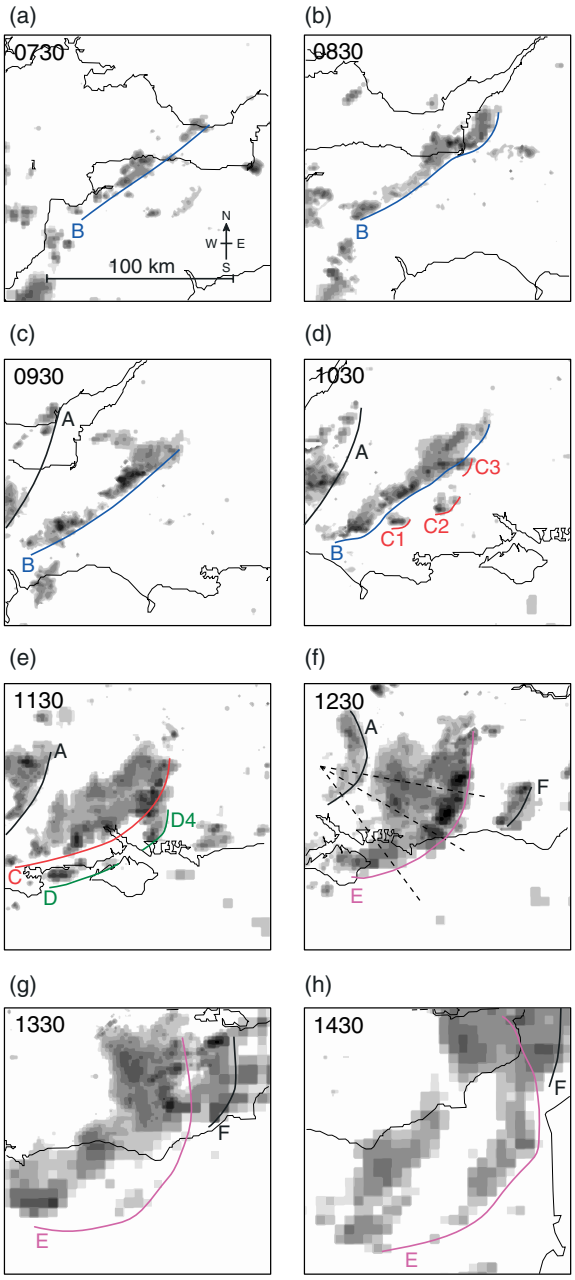

Figure 12. Network radar rainfall rates (composite of 1, 2 and 5 km products) at hourly intervals from 0730 UTC to 1430 UTC on 25 August 2005 over a domain moving with the MCS (see text for detail). The grey scale is logarithmic as in Figure 11, and peak rates are greater than 32 mm h^{-1}; note the transition to 5 km data over coastal area. Lines show the leading edge of convection lines derived from radar rainfall and MSG HRV imagery. Black dashed lines in (f) show positions of RHI scans in Figure 8(g–i). This figure is available in colour online at wileyonlinelibrary.com/journal/qj

'bulge' in Line B at it's northern end is also due to a cell, C3, which developed close to, but ahead of, Line B from about 1015 UTC, but at this stage cannot be distinguished from Line B. We shall discuss the mechanism for the development of Line C in more detail below in section 7.2.

Figure 12 shows the broad time sequence of radar-derived rainfall rate. The domain is centred along line MN in Figure 14, starting at the western end of the line and tracking the system with a speed of 13 m s^{-1} (so that any apparent propagation from frame to frame is relative to this velocity; this was chosen as it is approximately the propagation speed of the coldest part of the cold pool). Also indicated are lines

showing the leading edges of the lines of showers (A, B, C, D, E and F) forming part of the MCS. These are based primarily on the rainfall signal but also (especially in later frames, where the line is no longer precipitating in some parts) from the leading edge of cloud derived from the MSG high-resolution visible image (HRV). This evolution is summarised in Figure 14 (including data from 1100 UTC shown in Figure 9(b)).

The dominant feature of the MCS from 0730 UTC until 1030 UTC was Line B, with the weaker Line A behind it. The system underwent a complex transition between about 1030 UTC and 1130 UTC which will be discussed in more detail in section 7. At 1030 UTC, three cells mentioned above (C1, C2 and C3) had formed ahead of Line B. By 1130 UTC Line B had essentially disappeared as a distinct line, the remnants forming a region of less intense rain behind Line C. Meanwhile, new cells were developing ahead of Line C, forming a somewhat broken line (labelled D and D4 in Figure 12(e)). By 1200 UTC, Lines B, C and D had merged into one system, with a distinct line of intense showers (Line E) leading a broad area of less intense rain (the residue of Line B). Another line, F, is identified ahead of Lines C and E from 1230 UTC. This comprises cells which formed along the eastern part of the sea-breeze convergence line that triggered Line D (section 7 below), though the F cells triggered somewhat later than the D cells. From 1230 UTC onwards, the northern part of the MCS remained over land, with Line E continuing to produce intense rainfall while the southern part of Line E developed the arc cloud and bow echo discussed above. At 1330 (Figure 12(g)) Line E shows little or no rain over the sea, though it is extremely clear in the MSG imagery (Figure 6(b)), while the weaker rain from the remnants of Line B (and, perhaps, C) are distinctly separate behind Line E. Precipitation from Line E appears to have strengthened as it approached the French coast at 1430 (Figure 12(h)), though this could be an artefact of the radar processing.

Line E moved at about $16\,\mathrm{m\,s^{-1}}$ along the line MN in Figure 14, until it reached the coast at about 1310 UTC. This increase in propagation speed may be associated with an increase in the depth of the cold pool resulting from the increase in extent and intensity of precipitation around 1200 UTC. After it reached the coast, Line E was weaker but moved at up to $19.3\,\mathrm{m\,s^{-1}}$ along MN. This last increase in speed is presumably, at least in part, due to it encountering less friction over the sea (and also, therefore, stronger ambient boundary-layer winds).

In the context of two-dimensional squall lines, the initial wind profile resembles the constant shear case of Thorpe *et al.* (1982), which does not lead to a long-lived system. However, since the initial Line B is approximately aligned with the strong shear vector and there is some low-level shear between the surface and about 900 hPa with component normal to the line, it is likely to be more helpful to discuss the structure in terms of the 'parallel stratiform' systems identified by Parker and Johnson (2000) and analysed in more depth by Parker (2007b). In fact, the wind profile has much in common with the control simulation of Parker (2007a). Such systems occur when the initial line convection is aligned with a strong upper-level shear, with the result that, at least initially, the stratiform region forms along and to some extent downstream of the initial line. Eventually, cold-pool dynamics (and, probably, gravity-wave dynamics) leads to lateral development of the system. Parker (2007b) shows that the low-level shear is necessary to oppose the propagation of the cold pool relative to the storm; indeed, as discussed above, it is likely that the combination of strengthening cold pool and reduced low-level shear over the sea results in the cold pool eventually running ahead of the system.

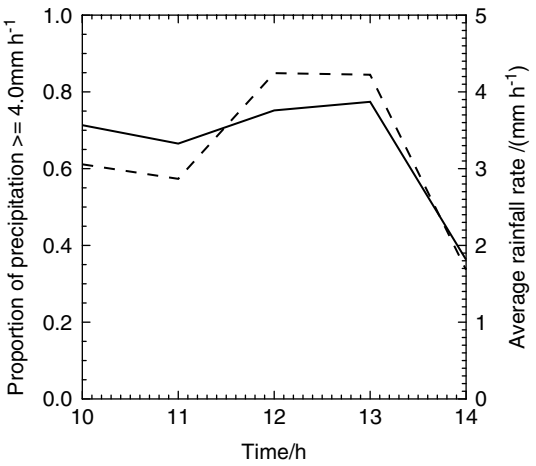

Figure 13. Analysis of network radar rainfall rates (composite of 1, 2 and 5 km products) at hourly intervals 1000 to 1400 UTC on 25 August 2005 identified as part of the MCS. Solid line (left-hand scale) gives the proportion of the total rainfall provided by rates over 4 mm h^{-1}. Dashed line (right-hand scale) shows the average rainfall rate where above 0.05 mm h^{-1}.

The system evolves broadly in the same way as the parallel stratiform systems studied by Parker (2007b), in particular, the initial linear system evolves into a distinctly 3D system, dominated by (backbuilding) convection at the upshear end and with an increasing component of stratiform precipitation downshear, gradually developing trailing stratiform characteristics. However, the overview above shows a complex transition phase between about 1030 and 1200 UTC from the initial linear system to a more intense phase which sets the scene for the development of the rapidly propagating cold pool with the arc cloud and bow echo at its leading edge.

Figure 13 shows an analysis of the network radar rainrates to give some measure of the convective (or, at least, high-intensity) component of the MCS precipitation. The relatively low stratiform component is consistent with the parallel-stratiform nature of the system. Perhaps surprisingly, the figure shows a small increase in convective component during the system transition phase; even though the stratiform region behind the system had clearly developed in area, the convective rainfall rate also intensified. Only after transition to Line E, and its weakening as it propagated over the sea, did the convective component dramatically decrease.

The next section describes the transition phase in more detail in an attempt to identify the processes operating during the transition.

7. Detailed analysis of transition to the intense phase of the MCS

Figure 15 shows radar data every 15 min during the transition period, together with information about the AWS and SYNOP sites that give an indication of the timing of the passage of the cold pool. The leading edge of convection

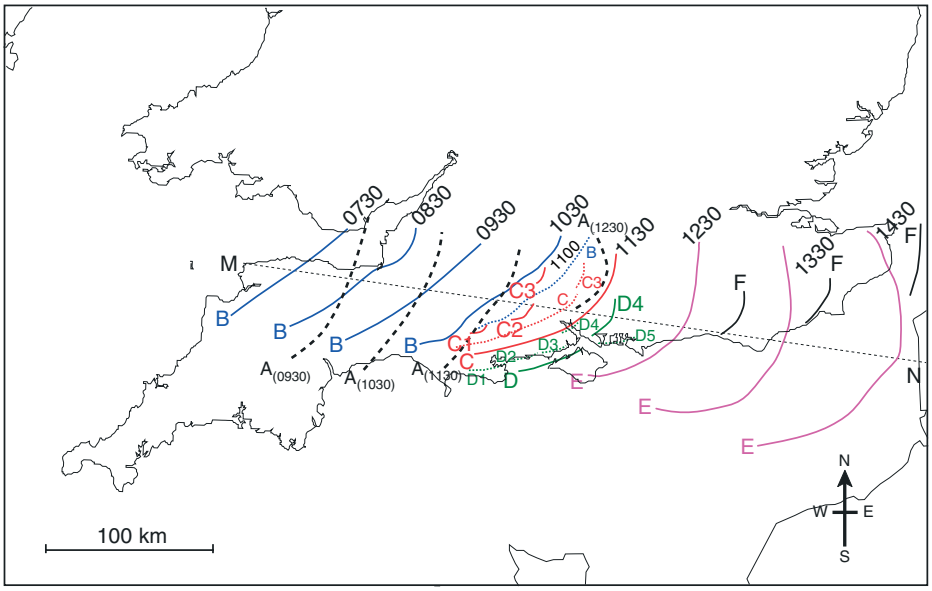

Figure 14. Evolution of the leading edge of the MCS derived from operational radar rainfall and MSG HRV imagery. Lines are shown every hour, on the half hour; Line A is indicated by thick dashed and Lines B, C, D, E and F by solid lines. Also shown (dotted) is the leading edge of shower lines at 1100 UTC. See text for the identity of Lines A, B, C, D, E and F. The thin dashed line, MN, shows the line along which the centres of panels in Figure 12 are located. This figure is available in colour online at wileyonlinelibrary.com/journal/qj

lines, derived from radar and MSG imagery, is also shown by dotted lines as in previous figures.

In total, 17 surface stations (AWS and 10 min SYNOP sites) provided very clear indications of the passage of a substantial surface cold pool. Examples of the temperature traces from surface sites are shown in Figure 16. Here, three groups have been identified based on latitude. Each group is shown by lines connecting station locations on Figure 15. The three groups show similar behaviour across the group, although with differences in detail. Figure 16 also shows station H, located to the south of the southern group.

The stations in the northern group show a relatively gentle rate of temperature drop with the arrival of the cold pool, taking about half an hour to reach a distinct minimum from the onset of the drop. A second cold pool associated with Line A is also evident an hour behind the first, though this becomes increasingly less distinct with time (i.e. at stations further east), due to the backward spread of the main cold pool relative to the leading edge. The slow drop in temperature in the northern group of AWS stations corresponds to the passage of the more diffuse region of rain at the northern end of Line B as opposed to the sudden drop encountered at the leading edge further south where the main intensification occurred.

7.1. The cold pool and the triggering of Lines C and D

The central group of stations in Figure 16 shows similar features to the northern group but with a greater and more rapid temperature drop. The cold pool due to Line A is still evident but it is weaker than the leading cold pool, and merged with it. From Figure 15 it is evident that the cold pool arrival at station E, at the western end of this group, corresponds to the outflow from Line B.

The next two stations are less clear; the initial arrival at W, at 1030 UTC, corresponds to the Cell C3 which formed ahead of Line B (with first indication on radar at 1015 UTC). The decrease in temperature is slower than at station E (though this may, in part, be an artefact of the 10 min data) and the lowest temperature is reached from 1100 UTC, corresponding to Line B. There is a suggestion of a double temperature drop at station C, the initial drop at about 1045 UTC corresponding to Cell C3 and the remaining drop, at about 1110 UTC corresponding with the cold pool due to Line B. The analysis shown in Figure 9 suggests a delay in the arrival of the cold pool between Cell C3 and the rest of Line C, initially identified as Cells C1 and C2. It is possible that the portion of the surface cold pool generated by Cell C3 was initially distinct from that further south. This gap in Line C persisted for some time (until about 1120 UTC). RHI scans from Chilbolton (station C) at azimuths 189°, 168° and 143° at 1103, 1105 and 1107 UTC respectively (Figure 8(c–a)), all show the nose of a low-level jet having progressed about 10 km beyond Chilbolton, with intense precipitation ahead (10–20 km from Chilbolton) corresponding to Line C. Thus, at 1100–1110 UTC at least close to Chilbolton, the low-level jet extends ahead of Line B but behind Line C precipitation.

The southern group of two stations provides the clearest evidence of a contiguous cold pool with Line C at its leading edge. The site further east (site D) shows an extremely rapid temperature drop (about 7 °C in a few minutes) with the arrival of Line C shortly after 1100 UTC. (The most rapid temperature drop occurs at 1108 UTC at site D, so site D is identified on Figure 15(d) rather than Figure 15(c) but it is clear that the initial temperature drop corresponds to the leading edge of Line C.) The other station (P) shows a similar overall drop, but in two stages separated by about 25 min. The initial drop at station P started at about 1040 UTC, and corresponded to Cell C2. The second drop started at about 1100 UTC and lay behind the leading edge of Line C but still distinctly in front of Line B. By this time there was weaker precipitation between Lines B and C. Figure 15(c) suggests that the second drop was associated with the northern edge of another cell within Line C.

The arrival of the cold pool at station H at 1115 UTC also corresponded with the arrival of the southern end of Line C (also Figure 15(d)). Cells D1 and D2 were developing

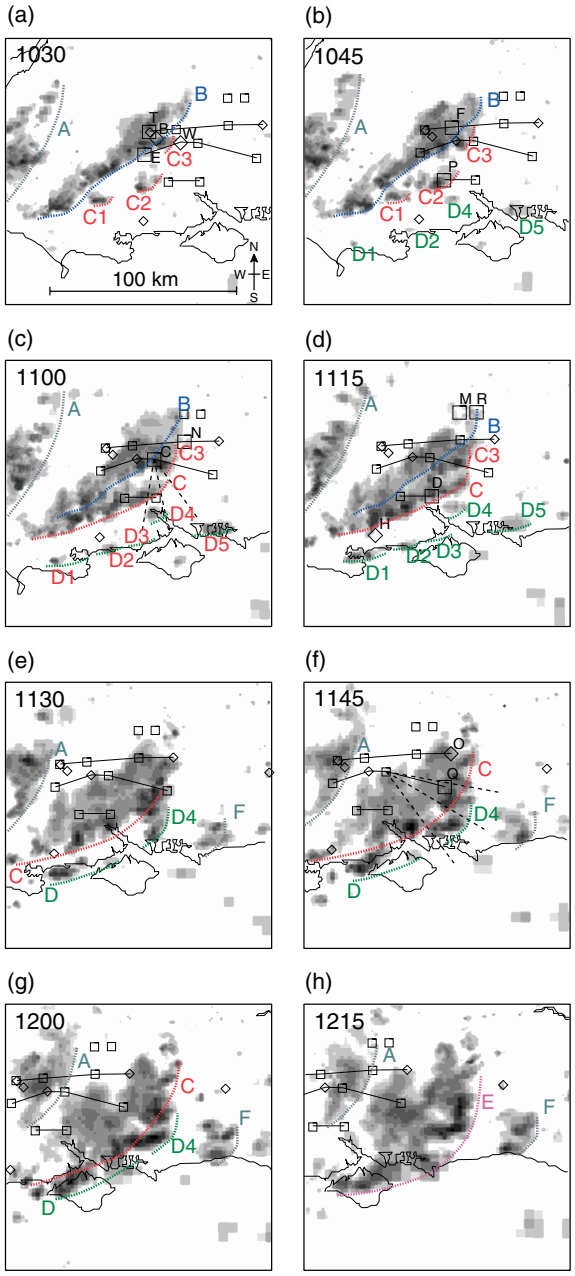

Figure 15. Network radar rainfall rates (composite of 1, 2 and 5 km products) at 15 min intervals from 1030 to 1215 UTC on 25 August 2005 over a domain moving with the MCS (see text for detail). The grey scale is logarithmic as in Figure 11; peak rates are greater than 32 mm h^{-1}; note transition to 5 km resolution data near coastal area. Dashed lines with larger letters represent the leading edges of the lines of convection identified in the text. Also marked are locations of AWSs (squares) and 10 min SYNOP stations (diamonds). These symbols are shown large with smaller site letter in frames where the time of maximum rate of drop of temperature is within 8 min of the time of the frame. Northern, Central and Southern Groups of surface stations shown in Figure 16 are joined by thin black lines. Straight dashed lines in (c) and (f) show positions of RHI scans in Figure 8(a–c) and (d–f) respectively. This figure is available in colour online at wileyonlinelibrary.com/journal/qj

ahead of station H at this time but were probably too far ahead and too immature to have contributed to the observed temperature drop at H. This temperature drop is noticeably smaller (by about 3 °C) than those in the southern group and the pressure perturbation (Table 1) is also smaller. It is worth noting that the southern end of Line C intersected Line B and it is very difficult to distinguish the two; it is possible that the bulge at the southern end of Line B at 1030 and 1045 (Figure 15(a, b)) is actually a cell forming part of Line C.

To conclude our interpretation of the cold pool in relation to Lines B and C, the cold pool clearly propagated ahead of Line B with an orientation close to that of Line C and there is a strong association between the timing of arrival of the leading edge and the arrival of precipitation from Line C. (This is true also of the northernmost end of Line C at station Q; Figure 15 is slightly misleading in this case, as the time of most rapid temperature drop lies midway between frames (e) and (f) and Figure 16 shows that the temperature started to fall close to 1130 UTC, Figure 15(e)). It would appear that Cells C1, C2 and C3 formed a little ahead of the cold pool formed by Line B. The cold downdraughts from each new C cell left behind cold air at the surface which merged with the advancing cold air from Line B and so the leading edge of the cold pool jumped ahead of the Line B cold pool. The Line C cells were not triggered directly by the arrival of the cold pool from Line B, but it is possible that they may have been triggered by the effects of gravity waves generated by Line B in a manner similar to that reported by Morcrette *et al.* (2006), who analysed a case from the CSIP pilot study (also Fovell, 2002; Fovell *et al.*, 2006).

The observations demonstrate that Line D, already evident as new cells in Figure 15(b) at 1045 UTC, lay well ahead of the cold pool and was not directly associated with it. This line was probably part of a longer line of cloud which had formed just inland from Poole in the west to Herstmonceux in the east. This is typical of clouds forming on a sea-breeze convergence line (Bennett *et al.* (2006)). The eastern half of this line was not precipitating at this time but produced precipitation later. The cells D1–D5 have been identified as being related as they all form at a similar time on (presumably) the sea-breeze convergence line. However, they did not all share the same fate. The cells of Line D all moved towards the east but those closer to the MCS (D1–D4) were overtaken by Lines B and C and their associated cold pool, eventually merging with them to become the dominant line between 1200 and 1230 UTC. This emerging line is labelled E (Figure 15(h) and Figure 12(f)) to emphasise the merging process. Cell D5 was too far east to be overtaken and it eventually developed into a significant cluster in its own right, Line F. A separate shower had also triggered across the Solent on the Isle of Wight (Figure 15(c)), probably due to the Isle of Wight's own sea breeze convergence, but this weakened as it moved east over the sea (Figure 15(e)).

To summarise this section, the transition phase between 1030 and 1215 UTC corresponded to the formation of two distinct lines of showers ahead of the initial linear system. In each case the cold pool, which was travelling faster than the individual cell velocity, merged with cold downdraughts from the new showers leading to a discontinuous propagation of the system. One of these lines is likely to have formed independently of the MCS, very probably on a sea-breeze convergence line. The mechanism for formation of the other is unknown, but it is possible that it was triggered by ascent associated with gravity waves generated by the MCS.

7.2. Time evolution of the temperature and propagation speed of the cold pool

In section 5 the propagation velocity of the cold pool was derived from the magnitude of the maximum surface

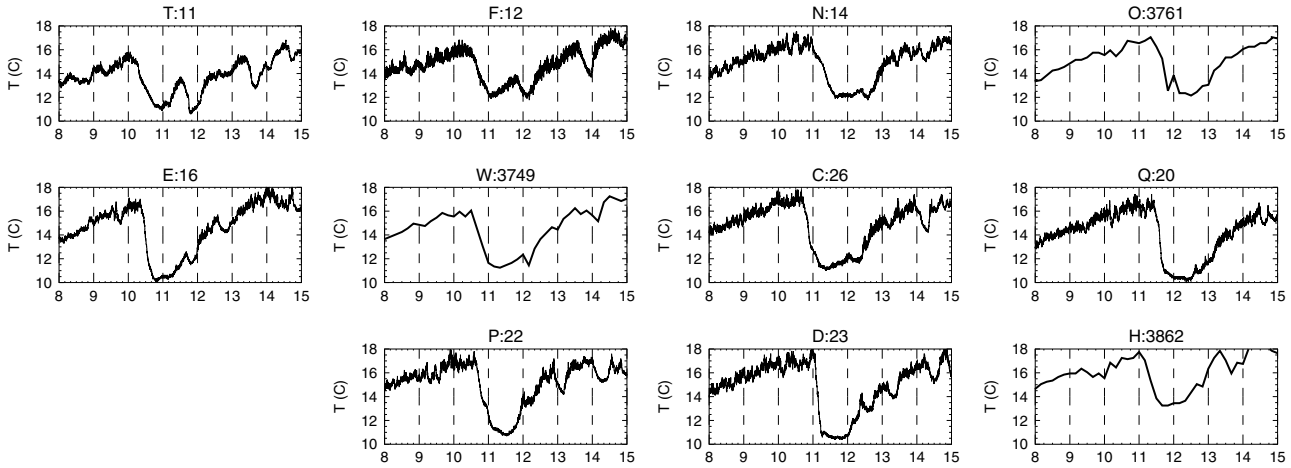

Figure 16. Time series of temperature from AWS and SYNOP sites. Top row: northern group. Middle row: central group. Bottom row: southern group and site H. Frame headings indicate site letter and site number. Note that SYNOP sites (H, O and W) provided data every 10 min, and data from other sites are 1 min averages.

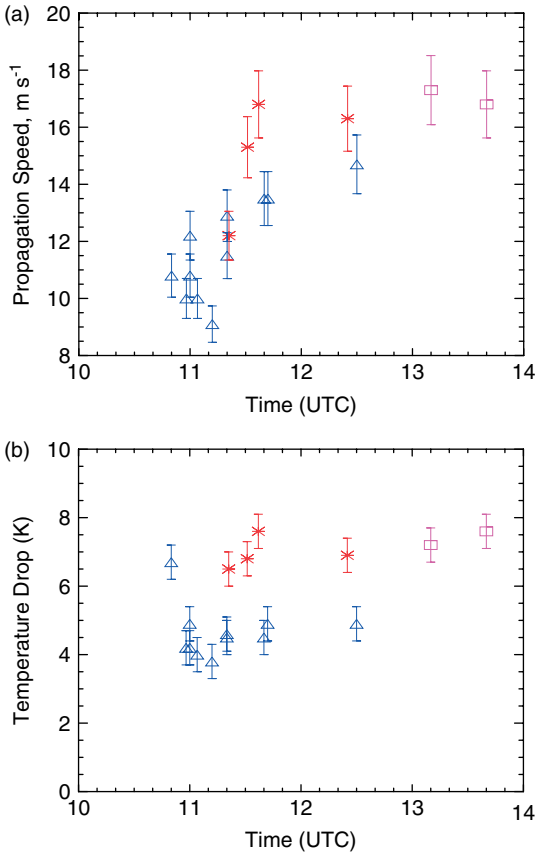

Figure 17. Time series of (a) cold-pool propagation speed estimated from magnitude of the maximum surface pressure increase and (b) temperature drop in the cold pool from AWS and 10 min SYNOP data. Symbols denote the convective line responsible for the cold pool: Line B (triangle), Line C (asterisk) or Line E (square). This figure is available in colour online at wileyonlinelibrary.com/journal/qj

pressure increase at different surface stations. These estimates were shown earlier in Table 1 and are plotted in Figure 17(a) as a function of the time of most rapid temperature drop. Though somewhat variable, there is a clear tendency for the derived propagation speed and so the associated magnitude of the pressure rise to grow in time, the speed growing from 10–12 m s^{-1} to above 16 m s^{-1}. The absolute value of the propagation speed depends upon assumed constants and assumptions about the impact of ambient flow (the latter not included here as it represents just a constant offset), but the trend of the data does not. Figure 17(a) shows the strongest trend of increasing propagation speed between about 1030 and 1130 UTC, during the transition phase portrayed in Figure 15, with a levelling off after this at about 16–18 m s^{-1}. We have no data prior to 1030 UTC, so it is possible the increasing trend existed earlier. Examination of which line of convection corresponds to each station suggests that the increase is primarily in Line B, whereas the data points corresponding to Lines C and E (with one exception) contribute the later, more constant and high propagation speeds to the timeseries.

There is not such a clear indication of a corresponding trend in surface temperature drop with time (Figure 17(b)). However, the data do appear to cluster into two groups, with 4–5 and 6–8 °C drops respectively. Table 1 indicates which convection line corresponds to the leading edge of the cold pool at each site. This shows that the two groups in Figure 17(b) correspond to Line B on the one hand, and Lines C and E on the other. With the exception of station E plotted at 1050 UTC, the original Line B gave rise to smaller temperature drops than Lines C and E which formed during the transition to the intense phase.

To summarise this section, surface observations show a clear trend for increasing pressure perturbation (and, hence, cold-pool propagation speed) in Line B through the transition phase. The change in the magnitude of the drop in temperature with time was relatively small compared with the corresponding change in pressure rise, suggesting that the increasing trend in pressure rise was due more to an increase in depth than in temperature drop. Lines C and E had a faster propagation speed and larger temperature drop compared with the initial Line B. Model simulations in Part 2 suggest that the transition corresponds to a change to a more rearward sloping flow, with a contribution to increased system propagation speed coming from the development of a weak rear-inflow jet, the growth of which may be associated with the increase in the derived cold-pool propagation speed.

7.3. *Evolution of the depth of the convective boundary layer*

Further insight into the transition period can be gained from analysis of the depth of the convective boundary layer (CBL)

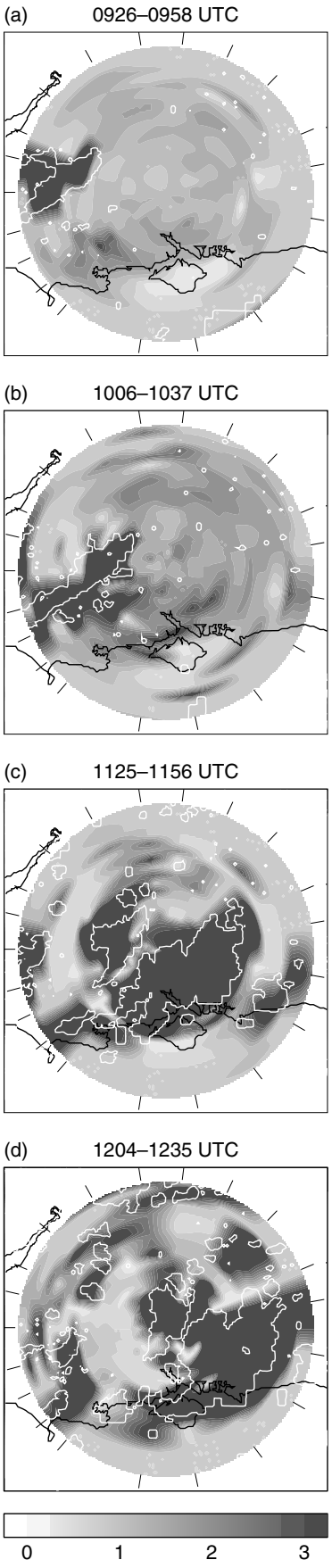

Figure 18. Analysis of maximum depth of convection (km) obtained from CAMRA 3 GHz radar RHIs. The maximum range of the radar data is 95 km. Time periods are marked on figures, and the location of RHIs marked by radial lines. Overlaid white contours correspond to instantaneous network radar rate of 0.125 mm h^{-1} at (a) 0945, (b) 1015, (c) 1145 and (d) 1215 UTC.

in the precipitation-free environment surrounding the MCS derived from the CAMRA 3 GHz radar at Chilbolton. Convective cells are evident even in the absence of precipitation, largely due to Bragg scattering from refractive index inhomogeneities due to strong moisture gradients, in particular at the top of thermals. The maximum depth of convection has been derived over 5 km bins from RHI scans obtained at roughly 20° intervals of azimuth. The depth of the CBL cannot be determined in this way in the presence of precipitation; however, precipitating regions have been interpreted as regions of very deep mixing, even though it is likely that in places decaying convective cells or layer cloud were precipitating into a shallow boundary layer. The data are therefore more reliable away from precipitation.

Two-dimensional plots have been derived from these by bilinear interpolation in polar coordinates (Morcrette *et al.*, 2007). A sequence of scans around 360° azimuth took about half an hour (moving anti-clockwise from north), so some development and advection occurred during a sequence of scans, but the main features appear consistent with other available information. Figure 18 shows analyses for four times. The first ((a), 0926–0958 UTC) shows the MCS to the west of Chilbolton (compare with Figure 12(c) at 0930 UTC). Elsewhere there is a fairly uniform CBL depth up to about 1.5 km. However, the CBL appears deeper in a fairly continuous region along the coast, with a region to the southwest of Chilbolton quite close to the coast where it extends above 2 km, with a peak around 3 km near where Cell C2 was eventually triggered. There is also a suggestion of a shallower CBL off the coast (and, perhaps surprisingly, over the Isle of Wight).

The next cycle of scans ((b), 1006–1037 UTC) shows the deep Cells C1 and C2 (two of the new cells shown in Figure 11) ahead of the main Line B. Deeper CBL depth is also evident close to the south coast. This is the early stages of Line D which we suspect is due to coastal convergence; however, the position and orientation does not conclusively demonstrate a coastal influence, as the overall region of deeper CBL appears orientated in a similar direction to Line B, and a second region of deeper CBL appears downstream over the channel. This orientation may be an artefact of the analysis, which inevitably tends to produce structures orientated circumferentially around Chilbolton. Looking at the deeper CBL regions actually along the scans gives more confidence that they are associated with the coast (and the western end of the Isle of Wight).

Figure 18(b) also shows an indication of suppression of the depth of the CBL to below 1 km behind Line B between about 60 and 80 km to the westnorthwest of Chilbolton. This is also evident in Figure 18(c), between 1125 and 1156 UTC, though by now the MCS precipitation covers a wide area. (The sequence of scans between (b) and (c) is not shown for reasons of space – it essentially shows the same features as (b) and/or (c)). Suppression of CBL depth is also very evident behind Line A to the west of Chilbolton in Figure 18(c). The leading edge of the MCS to the southeast of Chilbolton is of particular interest, as there appears to be a region of deep CBL just off the coast ahead of the main region of precipitation. We interpret this as convective mixing deepening close to the leading edge of the cold pool as it began running ahead of the MCS. The showers that form Line F are also evident as a region of deeper CBL to the east of the frame close to the coast. Finally, Figure 18(d) (1204–1235) shows that in the region affected by the cold

pool behind the MCS (and behind Line A) the CBL is very shallow ($\sim$ 750 m) despite this being close to the peak of the diurnal cycle.

In summary, examination of the maximum depth of non-precipitating convection from the CAMRA 3 GHz radar shows that the Line D showers initiated in an area of deeper convection along the south coast well ahead of the MCS. It also shows the strong suppression of convective mixing in the cold pool behind the MCS, consistent with the absence of cloud evident from satellite imagery (e.g. Figure 6), and some evidence of the cold pool propagating ahead of the MCS towards the end of the transition period.

8. Discussion and conclusions

The widespread convection observed during CSIP IOP 18 on 25 August 2005 corresponded to the passage of an upper-level PV anomaly and associated cold anomaly below the tropopause over relatively high-θ_w air near the surface. Convection was initially possible when an inhibiting 'lid' disappeared between 0800 and 1000 UTC.

An initial line of showers formed with orientation along the wind shear vector between 850 and 500 hPa, and hence approximately perpendicular to the upper-tropospheric temperature gradient. The orientation was also roughly along the coast. It was therefore probably initially organised by the structure of upper-level instability but also possibly aided by convergence at the coast. This line went on to form a long-lived MCS. This was associated with a large surface cold pool (with at least 6–7 K surface temperature perturbation) beneath an extensive region of precipitation behind the leading edge of the MCS. The system propagation speed was similar to, but veered 15–20° from, the wind speed ahead of the system at about 700 hPa, close to the middle of the unstable layer, though about 2 m s^{-1} faster than and similarly veered from individual cell propagation velocities. The leading edge of the cold pool corresponded with a low-level jet (and gust front) with peak wind speed 5–6 m s^{-1} greater than the system propagation speed. The low-level jet was fed by a downward-sloping rear-inflow jet from at least 65 km behind the gust front. Above this were rearward-sloping updraught regions. Cold air remained at the surface well behind (typically 100 km) the gust front, suppressing boundary-layer convection for several hours.

The system velocity is close to the ambient wind at mid-levels. It is also similar to the propagation velocity of the cold pool estimated from radiosonde temperature profiles and from surface pressure perturbations using standard relationships for density currents. This suggests the system is promoted by an approximate matching of mid-level and cold-pool propagation speeds as discussed by Rotunno *et al.* (1988). A match better than within 3 m s^{-1} cannot be certain, as it is difficult fully to take into account the ambient flow in the density-current relationships. However, it is likely that the matching is not perfect and there is evidence for both acceleration of the cold-pool propagation speed and unsteadiness in propagation through generation of new lines of convection ahead of the leading edge.

Though relatively small, the system broadly follows the structure of linear MCSs discussed by Houze (2004). In particular, consistent with the strongly sheared environment, it has much in common with the parallel stratiform systems of Parker and Johnson (2000) and Parker (2007b) which develop three-dimensional structure due to the propagation of the cold pool perpendicular to the upper-level shear. However, the development of the observed system appears to have some differences.

In particular, a complex transition phase occurred between 1030 and 1200 UTC from the initial linear system to a more intense phase which set the scene for the development of the rapidly propagating cold pool with an arc cloud and bow echo at its leading edge. The transition phase corresponded to the formation of two distinct lines of showers ahead of the initial linear system. In each case the leading edge of the cold pool, which was travelling faster than the individual cell velocity, merged with cold downdraughts from the new showers leading to a discontinuous propagation of the system. One of these lines formed independently of the MCS, very probably on a sea-breeze convergence line. The mechanism for formation of the other is unknown, but it is possible that it was triggered by ascent associated with gravity waves generated by the MCS. Surface observations show a clear trend for increasing surface-pressure perturbation through the transition phase, which led to a significantly faster propagation speed and larger temperature drop of the subsequent lines forming the MCS compared with the initial line. The merged cold pool was thus deeper and colder and eventually propagated faster than the original system, forming a bow echo and arc cloud as it propagated across the English Channel. Until the merger, the propagation velocity of the overall system had been controlled by a combination of the above mechanisms rather than simply by cold-pool dynamics.

As CSIP focussed on convective initiation, observations inevitably concentrated more on low-level processes, and this article has concentrated on initiation at the leading edge of the system by various mechanisms. The cold pool is a very dominant feature of the observations, and it certainly grows or propagates with the system. However, this does not prove that it drives the system propagation. Furthermore, the (weak) rear-inflow jet has been identified but its role in promoting propagation or development has not been determined. In Part 2 we use these observations to validate model simulations of the event and than use sensitivity studies based on microphysical processes to add some insight into these questions.

Acknowledgements

The authors would like to acknowledge the Natural Environment Research Council (NERC) and the Met Office National Meteorology and Public Weather Service Programmes for funding CSIP. We would like to thank all who took part in the CSIP observational campaign who are too numerous to mention. We also are grateful to the Met Office for provision of radar rain rate data and Eumetsat and the Met Office Autosat team for Meteosat-8 data. The project exploited new instruments available through the Universities' Facilities for Atmospheric Measurement (UFAM) which is funded by NERC. The Chilbolton Laboratory is managed by John Goddard and owned by the Council for the Central Laboratory of the Research Councils. Finally we would like to thank the reviewers of earlier forms of this article, two anonymous, the other Bill Cotton, for their helpful and constructive comments which we believe have significantly contributed to this article.

References

Bishop CH, Thorpe AJ. 1994. Potential vorticity and the electrostatics analogy: Quasi-geostrophic theory. *Q. J. R. Meteorol. Soc.* **120**: 713–731.

Benjamin TB. 1968. Gravity currents and related phenomena. *J.Fluid Mech.* **31**: 209–248.

Bennett LJ, Browning KA, Blyth AM, Parker DJ, Clark PA. 2006. A review of the initiation of precipitating convection in the United Kingdom. *Q. J. R. Meteorol. Soc.* **132**: 1001–1020.

Bernardet LR, Cotton WR. 1998. Multi-scale evolution of a derecho-producing MCS. *Mon. Weather Rev.* **126**: 2991–3015.

Browning KA. 1997. The dry intrusion perspective of extra-tropical cyclone development. *Meteorol. Appl.* **4**: 317–324.

Browning KA, Blyth AM, Clark PA, Corsmeier U, Morcrette CJ, Agnew JL, Ballard SP, Bamber D, Barthlott C, Bennett LJ, Beswick KM, Bitter M, Bozier KE, Brooks BJ, Collier CG, Davies F, Deny B, Dixon MA, Feuerle T, Forbes RM, Gaffard C, Gray MD, Hankers R, Hewison TJ, Kalthoff N, Khodayar S, Kohler M, Kottmeier C, Kraut S, Kunz M, Ladd DN, Lean HW, Lenfant J, Li Z, Marsham J, McGregor J, Mobbs SD, Nicol J, Norton E, Parker DJ, Perry F, Ramatschi M, Ricketts HMA, Roberts NM, Russell A, Schulz H, Slack EC, Vaughan G, Waight J, Watson RJ, Webb AR, Wareing DP, Wieser A. 2007. The Convective Storms Initiation Project. *Bull. Am. Meteorol. Soc.* **88**: 1939–1955.

Bougeault P, Binder P. 2002. The Mesoscale Alpine Programme. *WMO Bulletin* **51**: 14–17.

Bougeault P, Binder P, Buzzi A, Dirks R, Houze RA, Kuettner J, Smith RB, Steinacker R, Volkert H. 2001. The MAP Special Observing Period. *Bull Am. Meteorol. Soc.* **82**: 433–462.

Bryan GH, Rotunno R. 2008. Gravity currents in a deep anelastic atmosphere. *J. Atmos. Sci.* **65**: 536–556.

Clark PA, Browning KA, Forbes RM, Morcrette CJ, Blyth AM, Lean HW. 2013. The evolution of an MCS over southern England. Part 2: Model simulations and sensitivity to microphysics. *Q. J. R. Meteorol. Soc.* DOI: 10.1002/qj.2142.

Cotton WR, Bryan G, van den Heever SC. 2011. *Storm and Cloud Dynamics*. *International Geophysics* Volume 99. Elsevier: Amsterdam.

Cram JM, Pielke RA, Cotton WR. 1992. Numerical simulation and analysis of a prefrontal squall line. Part II: Propagation of the squall line as an internal gravity wave. *J. Atmos. Sci.* **49**: 209–225.

Droegemeier KK, Wilhelmson RB. 1987. Numerical simulation of thunderstorm outflow dynamics. Part I: Outflow sensitivity experiments and turbulence dynamics. *J. Atmos. Sci.* **44**: 1180–1210.

Fovell RG. 2002. Upstream influence of numerically simulated squall-line storms. *Q. J. R. Meteorol. Soc.* **128**: 893–912.

Fovell RG, Mullendore GL, Kim S-H. 2006. Discrete propagation in numerically simulated nocturnal squall lines. *Mon. Weather Rev.* **134**: 3735–3752.

Fujita TT. 1978. 'Manual of downburst identification for project Nimrod'. Satellite and mesometeorology research paper 156, NTIS PB-286048, Dept. of Geophysical Sciences: University of Chicago, IL.

Goddard JWF, Eastment JD, Thurai M. 1994. The Chilbolton Advanced Meteorological Radar: a tool for multidisciplinary atmospheric research. *Electr. Commun. Eng. J.* **6**: 77–86.

Golding BW. 1998. Nimrod: A system for generating automated very short range forecasts. *Meteorol. Appl.* **5**: 1–16.

Henry SG, Wilson JW. 1995. 'The automatic thunderstorm nowcasting system'. Preprints, 27th Conference on Radar Meteorology, Vail, CO. Amer. Meteorol. Soc: Boston, MA.

Hoskins BJ, McIntyre ME, Robertson AW. 1985. On the use and significance of isentropic potential vorticity maps. *Q. J. R. Meteorol. Soc.* **111**: 877–946.

Houze RA Jr. 2004. Mesoscale convective systems. *Rev. Geophys.* **42**: RG4003, DOI: 10.1029/2004RG000150.

Kingsmill DE. 1995. Convective initiation associated with a sea breeze front, a gust front and their collision. *Mon. Weather. Rev.* **123**: 2913–2933.

Lean HW, Clark PA, Dixon M, Fitch A, Forbes R, Halliwell C, Roberts NM. 2008. Characteristics of high-resolution NWP models for forecasting convection over the UK. *Mon. Weather Rev.* **136**: 3408–3424.

Lee ACL. 1990. Bias elimination and scatter in lightning location by the VLF Arrival Time Difference technique. *J. Atmos. Oceanic Technol.* **7**: 719–733.

Liu C, Moncrieff MW. 1996. A numerical study of the effects of ambient flow and shear on density currents. *Mon. Weather Rev.* **124**: 2282–2303.

Lombardo KA, Colle BA. 2012. Ambient conditions associated with the maintenance and decay of quasi-linear convective systems crossing the northeastern US coast. *Mon. Weather Rev.* **140**: 3805–3819.

Marsham JH, Parker DJ. 2006. Secondary initiation of multiple bands of cumulonimbus over southern Britain. Part II: Dynamics of secondary initiation. *Q. J. R. Meteorol. Soc.* **132**: 1053–1072.

Moncrieff MW, Miller MJ. 1976. The dynamics an simulation of tropical cumulonimbus and squall lines. *Q. J. R. Meteorol. Soc.* **102**: 373–394.

Morcrette CJ, Browning KA, Blyth AM, Bozier KE, Clark PA, Ladd D, Norton EG, Pavelin E. 2006. Secondary initiation of multiple bands of cumulonimbus over southern Britain. I: An observational case-study. *Q. J. R. Meteorol. Soc.* **132**: 1021–1051.

Morcrette CJ, Lean HW, Browning KA, Nicol J, Roberts NM, Clark PA, Russell A, Blyth AM. 2007. Combination of mechanisms for triggering an isolated thunderstorm: observational case-study of CSIP IOP 1. *Mon. Weather Rev.* **135**: 3728–3749.

Olsson PQ, Cotton WR. 1997. Balanced and unbalanced circulations in a primitive equation simulation of a midlatitude MCC. Part II: Analysis of balance. *J. Atmos. Sci.* **54**: 479–497.

Pandya RE, Durran DR. 1996. The influence of convectively generated thermal forcing on the mesoscale circulation around squall lines. *J. Atmos. Sci.* **53**: 2924–2951.

Parker DJ. 1996. Cold pools in shear. *Q. J. R. Meteorol. Soc.* **122**: 1655–1674.

Parker MD. 2007a. Simulated convective lines with parallel stratiform precipitation. Part I: An archetype for convection in along-line shear. *J. Atmos. Sci.* **64**: 267–288.

Parker MD. 2007b. Simulated convective lines with parallel stratiform precipitation. Part II: Governing dynamics and associated sensitivities. *J. Atmos. Sci.* **64**: 289–313.

Parker MD, Johnson RH. 2000. Organizational modes of midlatitude mesoscale convective systems. *Mon. Weather Rev.* **128**: 3413–3436.

Raymond DJ. 1984. A wave–CISK model of squall lines. *J. Atmos. Sci.* **41**: 1946–1958.

Raymond DJ, Jiang H. 1990. A theory for long-lived mesoscale convective systems. *J. Atmos. Sci.* **47**: 3067–3077.

Rotunno R, Klemp JB, Weisman ML. 1988. A theory for strong, long-lived squall lines. *J. Atmos. Sci.* **45**: 463–485.

Schmetz J, Pili P, Tjemkes S, Just D, Kerkmann J, Rota S, Ratier A. 2002. An introduction to Meteosat Second Generation (MSG). *Bull. Amer. Meteorol. Soc.* **83**: 977–992.

Schmidt JM, Cotton WR. 1990. Interactions between upper and lower tropospheric gravity waves on squall line structure and maintenance. *J. Atmos. Sci.* **47**: 1205–1222.

Simpson JE. 1987. *Gravity currents in the environment and laboratory*. 2nd ed. Cambridge University Press: Cambridge, UK.

Thorpe AJ, Miller MJ, Moncrieff MW. 1982. Two-dimensional convection in non-constant shear: A model of midlatitude squall lines. *Q. J. R. Meteorol. Soc.* **108**: 739–762.

Thorpe AJ, Bishop CH. 1995. Potential vorticity and the electrostatic analogy: Ertel–Rossby formulation. *Q. J. R. Meteorol. Soc.* **121**: 1477–1495.

Tompkins AM. 2001. Organization of tropical convection in low vertical wind shears: The role of cold pools. *J. Atmos. Sci.* **58**: 1650–1672.

Weckwerth TM, Parsons DB, Koch SE, Moore JA, LeMone MA, Demoz BB, Flamant C, Geerts B, Wang J, Feltz WF. 2004. An overview of the International H20 Project (IHOP-2002) and some preliminary highlights. *Bull. Amer. Meteorol. Soc.* **85**: 253–277.

Weisman ML. 1992. The role of convectively generated rear-inflow jets in the evolution of long-lived mesoconvective systems. *J. Atmos. Sci.* **49**: 1826–1847.

Weisman ML. 2001. Bow echoes: A tribute to T. T. Fujita. *Bull. Am. Meteorol. Soc.* **82**: 97–116.

Wilson JW, Mueller CK. 1993. Nowcast of thunderstorm initiation and evolution. *Weather and Forecasting* **8**: 113–131.

Wulfmeyer V, Behrendt A, Bauer H-S, Kottmeier C, Corsmeier U, Blyth A, Craig G, Schumann U, Hagen M, Crewell S, DiGirolamo P, Flamant C, Miller M, Montani A, Mobbs S, Richard E, Rotach MW, Arpagaus M, Russchenberg H, Schlüssel P, König M, Gärtner V, Steinacker R, Dorninger M, Turner DD, Weckwerth T, Hense A, Simmer C. 2008. The Convective and Orographically induced Precipitation Study: A research and development project of the World Weather Research Program for improving quantitative precipitation forecasting in low-mountain regions. *Bull. Amer. Meteorol. Soc.* **89**: 1477–1486.